Tunnelling and Underground Space Technology 100 (2020) 103389

Contents lists available at ScienceDirect

Tunnelling and Underground Space Technology

journal homepage: www.elsevier.com/locate/tust

Seismic response of subway station in soft soil: Shaking table testing versus numerical analysis

Weifeng Wu[a,b], Shiping Ge[a,c], Yong Yuan[a,*], Wenqi Ding[a], Ioannis Anastasopoulos[b,*]

[a] Department of Geotechnical Engineering, Tongji University, Shanghai, PR China
[b] Institute for Geotechnical Engineering, ETH Zürich, Switzerland
[c] Shanghai Shentong Metro Co., Ltd., Shanghai, PR China

ARTICLE INFO

Keywords:
Shake table testing
Finite elements
Seismic response
Soil-structure interaction

ABSTRACT

As revealed by the collapse of the Daikai Metro station during the 1995 Kobe earthquake, underground structures are not immune to seismic loading. Shanghai Metro operates 16 lines of 676 km length, comprising 413 underground stations. An additional 1000 km with 600 underground stations are planned for the next 20 years, calling for improved understanding of their seismic response. This paper studies the seismic performance of a typical 2-storey, 3-span Shanghai Metro station in soft soil, combining *shaking table testing* and *numerical modelling*. Notwithstanding scale effects, shaking table testing is performed to allow detailed simulation of the complex structural system of the station. The structure is modelled using granular concrete and galvanized steel wires to simulate the RC prototype. To remedy the problem of scale effects, *synthetic model soil* (a mixture of sand and sawdust) is used, along with similitude relations derived considering dynamic equilibrium. The properties of the *synthetic model soil* are adjusted to satisfy similitude; target stiffness and density are attained by adjusting the mixture proportions. To quantify the transferability of the results to prototype scale, the experiments are simulated with nonlinear finite elements (FE), modelling the *synthetic model soil* with a kinematic hardening constitutive model, calibrated against resonant column and direct shear tests. The FE model is shown to compare adequately well with the shaking table tests. The validated FE model is used to predict the seismic response of the *prototype*, thus allowing indirect transfer of the results from *model* to *prototype* scale. The model in prototype scale is calibrated for the real soil layers against in situ (down-hole) and laboratory (resonant column) tests. Moving from *model* to *prototype* scale, the racking deformation remains qualitatively similar. The racking drift is reduced by 50% going from *model* to *prototype* scale, which is partly due to scale effects, but also related to differences between the idealized soil of the experiments and the multiple soil layers encountered in reality. The maximum bending moment also reduces by 30% going from *model* to *prototype* scale. The base of the lower-storey columns is proven to be the most vulnerable section, as was the case for Daikai.

1. Introduction

Since the opening of its first metro line in 1993, Shanghai has seen a rapid development of subway systems, currently registering almost 10 million passengers per day. A total of 16 metro lines are currently operated by Shanghai Metro, having a total length of 676 km and comprising 413 underground stations (CAMET, 2019). In the coming 20 years, an additional 1000 km of metro lines will be constructed, along with roughly 600 new underground metro stations. Considering the significance to society and economy of such a vast underground transportation network, the evaluation of seismic risk of underground structures and tunnels and the development of rational seismic design methods becomes an issue of significance.

Underground structures are in general considered less vulnerable to seismic loading compared to overground structures (Owen, 1981). However, severe damage and even collapse of such structures have occurred in major seismic events (e.g., Kobe 1995, Chi-Chi 1999, and Düzce–Bolu 1999). One such dramatic example is the collapse of the Daikai metro station during the 1995 Kobe (Hyogoken Nambu) earthquake in Japan, which demonstrated that large underground structures may undergo considerable earthquake-induced deformation that may lead to their collapse (Iida et al., 1996). Several researchers have studied the collapse of the Daikai metro station (e.g., An et al., 1997; Huo et al., 2005; Iida et al., 1996; Ishibashi and Okamura, 1997), offering valuable insights on the seismic response of such underground structures. A potential explanation of the collapse is the combination of large

* Corresponding authors.
E-mail addresses: yuany@tongji.edu.cn (Y. Yuan), ioannis.anastasopoulos@igt.baug.ethz.ch (I. Anastasopoulos).

https://doi.org/10.1016/j.tust.2020.103389
Received 17 December 2019; Received in revised form 31 January 2020; Accepted 10 March 2020
0886-7798/ © 2020 Elsevier Ltd. All rights reserved.

Nomenclature

a [g]	Acceleration
a, b, n	Constants
C [kPa]	Initial kinematic hardening modulus, equal to E
C_u	Uniformity coefficient
c [kPa]	Cohesive strength of model soil
c' [kPa]	Effective cohesive strength
D_{a5-95} [sec]	Significant duration between 5 and 95% of Arias intensity
D_r	Relative density
d_{50} [mm]	Mean particle size
E [MPa]	Young's modulus
e	Void ratio
f'_c [MPa]	Compressive strength of the granular concrete
G, λ	Lame's constants
G_0 [MPa]	Initial shear modulus
$G_{0,m}$ [MPa]	Initial shear modulus of model soil
$G_{0,p}$ [MPa]	Initial shear modulus of prototype soil
G_s [kPa]	Secant shear modulus
h [mm]	Height of station cross-section
l [mm]	Length of station components in out-of-plane direction
M_{max} [kNm/m]	Maximum bending moment of underground structure
NF [Hz]	Natural frequency of vibration
p [kPa]	Earth pressure
PI	Soil plasticity index
S_A	Acceleration scale factor
S_F	Relative structural flexibility scale factor
S_G	Shear modulus scale factor
S_l	Geometry scale factor
S_S	Unit structural stiffness scale factor
S_ρ	Density scale factor
S_u [kPa]	Undrained shear strength
t [sec]	Time
T [sec]	Period
H [m]	Thickness of soil layer
u [m]	Displacement
v [m/s]	Velocity
v_s [m/s]	Shear wave velocity
w [mm]	Width of station cross-section
x, y, z	Cartesian coordinates
z [m]	Depth of soil
α	Backstress, describe kinematic evolution of yield surface
α_s	Magnitude of α at large plastic strains
γ_k	Variable determines rate of decrease of C
γ_0 [kN/m^3]	Unit weight
γ	Shear strain
Δ_1, Δ_2 [mm]	Inter-storey drift of upper- and lower-storey
δ [°]	Friction angle of soil-structure interface
ε [$\mu\varepsilon$]	Strain
ε_p [$\mu\varepsilon$]	Peak strain of the structure
ε_{max} [$\mu\varepsilon$]	Maximum strain across the structure
$\dot{\varepsilon}^{pl}$	Rate of plastic flow
$\dot{\bar{\varepsilon}}^{pl}$	Equivalent plastic flow rate
λ_0	Fraction of the maximum yield stress σ_y
ξ	Damping ratio
ρ [kg/m^3]	Density
σ [kPa]	Stress
σ_0 [kPa]	Yield stress
σ_0' [kPa]	Mean effective confining stress
σ_1, σ_2, σ_3 [kPa]	Principal stresses
σ_y [kPa]	Maximum yield stress at large plastic strains
τ [kPa]	Shear stress
Φ [mm]	Diameter of steel wire
φ [°]	Peak friction angle
φ' [°]	Effective friction angle
∇^2	Laplacian operator

shear loading due to racking deformation, with large axial loading due to large spans and overburden soil pressures, which led to brittle shear failure of the central columns. It should be noted that the station was built in the 60′s, according to obsolete seismic codes, without any of the modern provisions regarding capacity and ductility design.

In contrast to the collapsed one-storey section of Daikai station, a typical Shanghai metro station is a multilevel structure. Similar to Daikai, the cross-section of Shanghai metro stations comprises large spans, supported by intermediate columns (usually two). Although the external sidewalls of such underground structures can easily sustain the imposed seismic loads (if properly designed), as proven by the Daikai collapse, this is not necessarily the case for internal structural components, such as the intermediate columns and the corresponding beams and slabs. Due to their large cross-section dimensions, Shanghai metro stations typically comprise very thick (and therefore very stiff) sidewalls and slabs. Although such increased stiffness is mainly necessary for the static loads, its role on the seismic performance of the structure should be carefully considered. Seismic soil-structure interaction (SSI) is acknowledged to play a crucial role in this respect (Hashash et al., 2001).

Several relevant studies can be found in the literature, comprising experimental and numerical methods. Experimental (physical) modelling is necessary to derive insights on the role of SSI, but also to be used for validation of analytical and numerical methods (Stamos and Beskos, 1995). Reduced-scale physical modeling is most commonly applied. However, soil stiffness and strength are directly related to the confining stresses, and therefore scaling unavoidably leads to incompatibilities between model and prototype, so called "scale-effects" (Wood et al., 2002). Centrifuge modelling overcomes the problem of scale-effects by increasing gravity to recreate the same stress levels as in reality, and has therefore been used in several studies of tunnels (Chen et al., 2018; Cilingir and Madabhushi, 2011; Lanzano et al., 2015), foundations (Adamidis and Madabhushi, 2017; Loli et al., 2014), and also to study the effects of faulting on structures (Anastasopoulos et al., 2007). However, the applicability of centrifuge modelling has certain limitations when considering complicated large-dimension underground structures, due to capacity and size limitations. Even with a large beam centrifuge, scaling of the order of 1:100 would be necessary to model a typical station. Due to such limitations, centrifuge modelling campaigns typically focus on idealized "equivalent" cross-sections, omitting the details of the structural system.

In the case of the studied subway station, careful consideration of internal structural elements (columns and middle slabs) is necessary. In this context, 1 g reduced-scale shaking table testing is preferable. Taking advantage of the larger model dimensions (compared to centrifuge modelling), such testing offers the possibility to model the internal structural elements in adequate detail, and also to install more and better quality sensors. Naturally, in the absence of the centrifuge enhanced-gravity field, scaling becomes challenging. Several 1g scaling relations can be found in the literature, based on different assumptions (Roscoe, 1968; Iai, 1989; Yan et al., 2015). Using "synthetic" model soil (a mixture of sawdust and dry sand) has been proposed as (partial) remedy to scale effects (Yan et al., 2015). New scaling relations were introduced considering the synthetic soil, and a series of shaking table tests were conducted for long tunnels (Yan et al., 2015; Yu et al., 2018; Yuan et al., 2018; Chen et al., 2020a, 2020b), underground structure

joints (Zhang et al., 2019a, 2019b; Shen et al., 2020) and subway stations (Chen and Liu, 2019; Zhao et al., 2019).

Despite offering valuable insights, the use of synthetic soil and the corresponding scaling procedure have not been fully verified. Therefore, it is not fully understood to what extent the results of the 1 g shake table tests using synthetic soil can be considered transferrable to prototype conditions with real soil. Due to the unavoidable incompatibility between linear scaling relations and nonlinear soil behavior, a rational strategy to "convert" the results from model to prototype scale is required. Aiming to bridge the apparent gap in the literature, the present study conducts an experimental campaign, modelling a typical Shanghai metro station employing the "synthetic" soil technique. The 1 g shaking table experiments are then modelled with nonlinear finite elements (FE), assuming the properties of the synthetic soil (as measured through soil element tests). The validated (against the 1 g shaking table tests) FE modelling technique is then used to analyze the seismic response of the prototype problem. Employing such hybrid technique, the experimental results are indirectly (through the FE analysis) transferred from model to prototype scale.

2. Shaking table testing

The prototype problem is a typical Shanghai Metro station, currently under construction, part of Metro Line 14. As shown in Fig. 1, the studied reinforced concrete (RC) cut-and-cover station has a typical two-storey and three-span cross-section, with 13.82 m height, 23.2 m width, and 2 m soil cover. The slabs are supported by sidewalls and internal columns. In the out-of-plane direction, the columns have a longitudinal spacing of 9.1 m and are connected by longitudinal beams. As summarized in Table 1, with the exception of the first 1.9 m of artificial fill, the prototype soil profile consists of alternating layers of silty sand, mud clay, silty clay and sandy silt. The properties listed in the table are based on the geotechnical and geological exploration, in situ and laboratory tests. A total of 45 boreholes were conducted, including seismic down-hole, flat dilatometer and vane shear in-situ testing (CREEGC, 2014). Soil samples taken from 2 boreholes were used to conduct laboratory testing, including triaxial, resonant column and direct shear tests to measure soil properties.

Table 1
Prototype soil profile and key soil properties of the encountered layers.

No.	Soil	Depth z (m)	Thickness H (m)	Shear wave velocity v_s (m/s)	Unit weight γ_0(kN/m^3)	PI	c' (kPa)	φ' (°)
1	Fill	1.9	1.9	125	17.3	17	–	–
2	Silty clay	3.5	1.6	128	18.5	17	–	–
3	Silty clay	9.5	6.0	125	17.1	17	4	31
4	Mud clay	17.6	8.1	137	16.6	15	3	28
5	Clay	23.8	6.2	189	17.4	21	2	25
6	Silty clay	30.9	7.1	235	19.4	17	5	26
7	Sandy silt	42.8	11.9	255	18.9	15	7	33
8	Silt	50	30.9	322	18.9	–	–	–

2.1. Experimental setup and scaling relations

A series of 1 g shaking table tests were constructed at the multi-functional shaking table system of Tongji University. As depicted in Fig. 2**a**, two shaking tables are jointed together into a combined shaking table which is 10.1 m × 6.1 m in plan, and is capable of shaking up to 140 tons payload with a maximum acceleration of up to 1.5 g. The controlled frequency range is from 0.1 Hz to 50 Hz. Real seismic records, as well as synthetic motions can be simulated.

A new laminar box (Fig. 2**a**) was designed and constructed in order to conduct the experiments, with internal dimensions of 9.5 m × 5.5 m × 2.16 m (length × width × height). As shown in Fig. 2**b**, the laminar soil container consists of 16 steel frames, connected to each other by industrial ball bearings (Fig. 2**c**), which allow the

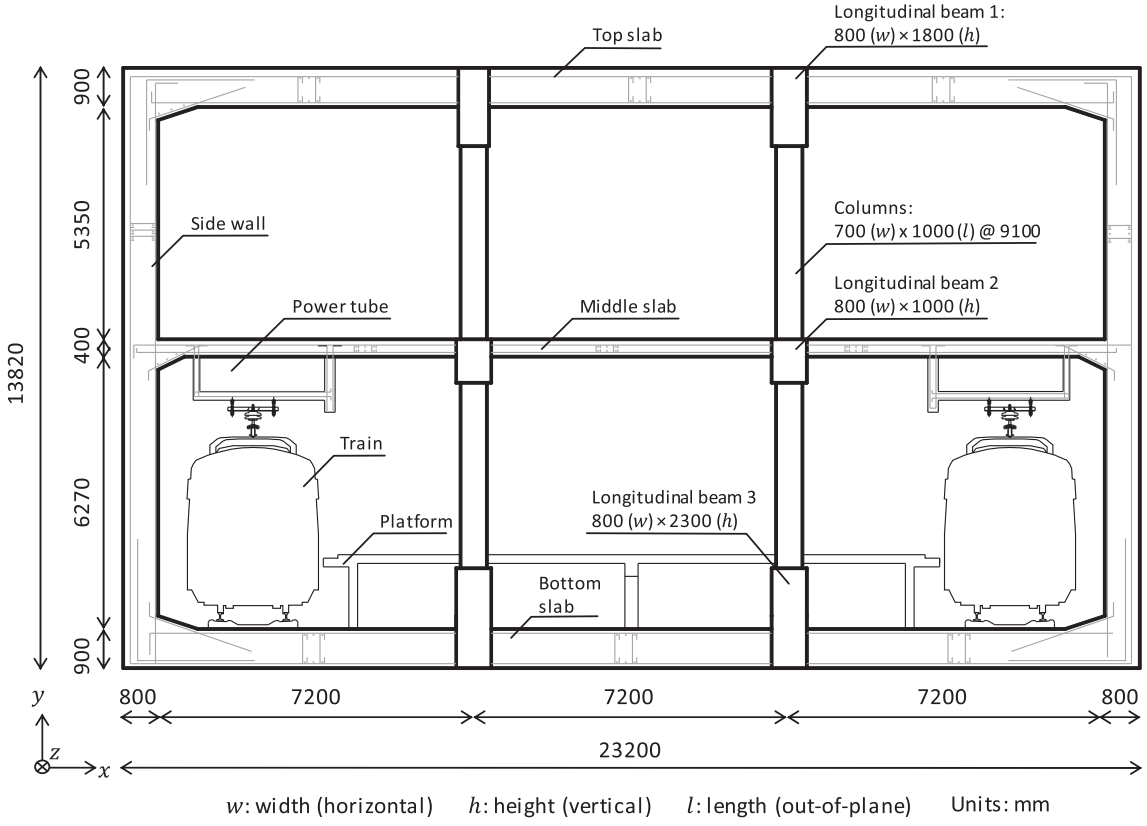

Fig. 1. Cross-section of the prototype problem of a typical 2-storey and 3-span Shanghai Metro station.

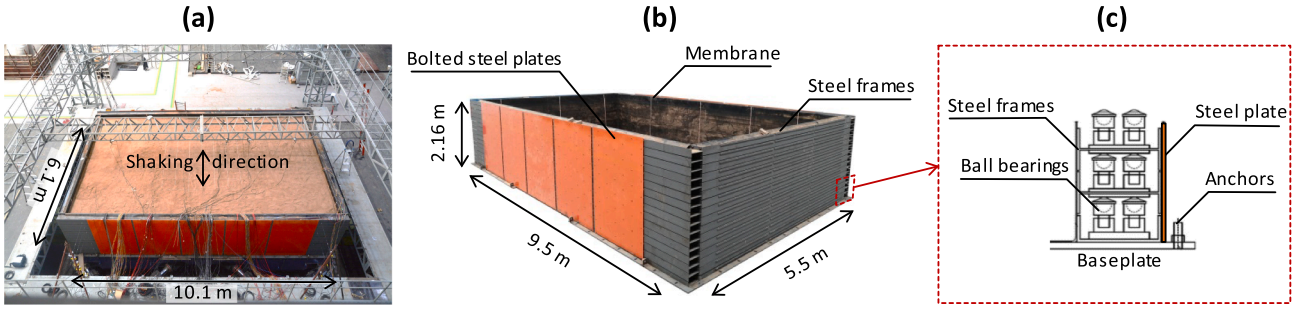

Fig. 2. Laminar box used for the shaking table tests: (a) overview of the soil container installed on the multi-functional shaking table of Tongji University; (b) key dimensions of soil container; and (c) detail of the sliders.

Table 2
Derived scaling relations (model soil) compared to Gibson, 1996 (prototype soil).

Quantity	Scale factor (Gibson, 1996)	Similarity relations of this study	"Designed" scale factor	"Actual" scale factor
Displacement(u)	S_l	S_l	1/25	1/25
Density(ρ)	–	S_ρ	1/2	1/2
Shear modulus(G_s)	–	S_G	1/50	1/48
Acceleration(a)	*1*	$S_G/(S_l S_\rho)$	1	1.04
Time(t)	$S_l^{0.5}$	$(S_l/S_a)^{0.5}$	1/5	1/5.1
Velocity(v)	$S_l^{0.5}$	$(S_a \times S_l)^{0.5}$	1/5	1/4.9
Shear wave velocity(v_s)	–	$(S_G/S_\rho)^{0.5}$	1/5	1/4.9
Frequency, dynamic(f)	$S_l^{-0.5}$	$(S_l/S_a)^{-0.5}$	5	5.1
Natural frequency(NF)	–	$(S_G/S_\rho)^{0.5}/S_l$	5	5.1
Force(F)	$\rho \times S_l^3$	$S_a \times S_\rho \times S_l^3$	1/31250	1/30048

frames to slide smoothly in the direction of shaking. Perpendicular to the shaking direction, two thin steel plates are bolted to the steel frames in order to avoid unexpected horizontal torsional movements. The FE simulations were conducted to validate dynamic response of the laminar container, based on which its maximum capacity, the allowable horizontal deformation, and its dominant modes of vibration were evaluated. Based on the results of the FE analyses, the thickness of the steel plates was set to 3 mm, so that the laminar container is flexible enough (to allow free deformation of the soil model), while the dominant mode of the box (of 1.2 Hz) does not interfere with the fundamental vibration modes of the soil model.

Taking account of the size and capacity of the shaking tables (combined), an $S_l = 1/25$ geometry scale factor was selected for the experiments. Since the experiments are conducted at 1 g (for the previously discussed reasons), similarity cannot be maintained by using the same soil material. An alternative approach is employed, replacing the *prototype* soil with a synthetic *model* soil (a mixture of sand with sawdust, as discussed later on).

Within this context, the remaining similitude factors are derived through combination of the Vaschy-Buckingham Π theorem, dimensional analysis (Langhaar, 1951), and dynamic equilibrium. To maintain similarity under dynamic loading, several requirements need to be satisfied. First of all, based on massive experimental observations, Kondner (1963) proposed that the nonlinear stress-strain response of soil could be described by the hyperbolic model:

$$\sigma_1 - \sigma_3 = \frac{\varepsilon}{a + b\varepsilon} \tag{1}$$

where: ε, σ_1 and σ_3 are the strain, major and third principle stress, respectively; and $a$and b are constants. Therefore, according to this simplifying assumption, the similarity ratio of strain can be derived as 1. Secondly, the dynamic equilibrium should be considered. Assuming the soil as a continuous medium, the unbalanced forces need to be balanced by the inertia force in the same direction. The dynamic equilibrium in the x-direction is:

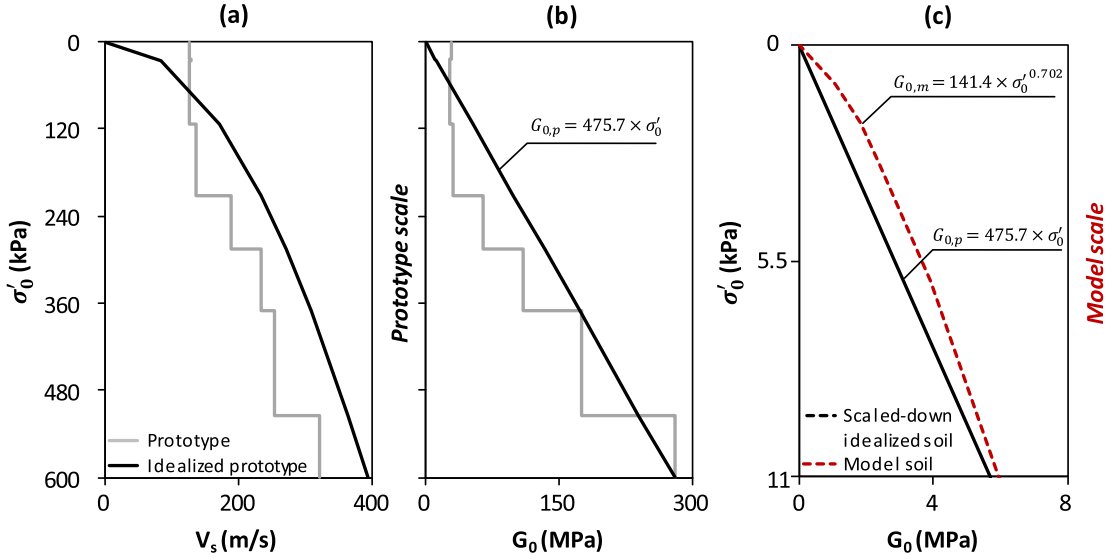

Fig. 3. From prototype (multi-layered) soil to synthetic (sand and sawdust) model soil. Distribution with confining pressure σ_0' of prototype vs. idealized prototype: (a) shear wave velocity v_s; and (b) small-strain shear modulus G_0; and (c) distribution of G_0 with σ_0 of scaled-down idealized soil vs. model soil (model scale).

Table 3
Measured small-strain shear modulus G_0 of *synthetic model soil* in function of confining pressure σ_0'.

Confining pressure σ_0' (MPa)	Small-strain shear modulus G_0 (MPa)
0.02	9.8
0.05	18.1
0.15	29.3
0.20	38.6

Estimated relation: $G_0 = 141.4 \times (\sigma_0')^{0.702}$ (MPa)

$$\rho\frac{\partial^2 u}{\partial t^2} = \frac{\partial \sigma_{xx}}{\partial x} + \frac{\partial \sigma_{xy}}{\partial y} + \frac{\partial \sigma_{xz}}{\partial z} \tag{2}$$

where: x, y, z are the Cartesian coordinates; ρ, t, u are density, time, and displacement in the x-direction, respectively (the same procedure can be applied to y and z). Eq. (2) is solely based on dynamic equilibrium, and is thus valid for any stress-strain relation (Kramer, 1996). Using Hooke's law, Eq. (2) can be written in terms of displacements:

$$\rho\frac{\partial^2 u}{\partial t^2} = (\lambda + G)\frac{\partial \varepsilon}{\partial x} + G\nabla^2 u \tag{3}$$

where: λ and G are the Lame's constants; and ∇^2 is the Laplacian operator. Eq. (3) specifies the interdependent relation between similitude ratios of density, shear modulus, displacement, and acceleration. It may therefore be deduced:

$$S_\rho = \frac{S_G}{S_a S_l} \tag{4}$$

where: S_ρ, S_l, S_G and S_a are similitude ratios of density, geometry, shear modulus, and acceleration, respectively.

In this study, the first three (S_ρ, S_l, S_G) are set as the basic scale factors, based on which an appropriate model material can be selected. Based on these three basic scale factors, the remaining scale factors can be obtained by applying the Vaschy-Buckingham Π theorem. The derived scaling relations using the previously described approach (using synthetic *model soil*) are summarized in Table 2, where they are compared to the typically employed scaling relations (using the *same soil* as in the prototype) (Gibson, 1996). Although the basic scale factors are different, if the synthetic *model* soil is selected appropriately, it is possible to maintain similitude in terms of acceleration $S_a = 1$. In this context, the final "designed" basic scale factors of geometry, density, and shear modulus are set to S_l= 1/25, S_ρ= 1/2, and S_G= 1/50, respectively. In addition, Table 2 also presents the "actual" (i.e., finally achieved) scale factor of the synthetic model soil, which is introduced in following.

2.2. Model soil

As previously discussed (see also Table 1), the prototype soil profile is muti-layered. Experimentally simulating the detailed layered soil profile is quite complicated and does not fall within the scope of this work. The *prototype* soil deposit is idealized as a single *model* soil layer with shear wave velocity v_s increasing parabolically with depth z ($v_s \sim z^{0.5}$), and therefore the shear modulus G_s increases linearly with the confining stress σ_0' ($G \sim \sigma_0'$). Such idealized soil profile has been used in several seminal publications (Ambraseys, 1959; Gazetas, 1982). The v_s distribution of the "*idealized prototype*" soil is selected by matching (on average) that of the *prototype* soil profile, as depicted in Fig. 3. The scaled-down *model soil* (Fig. 3**c**) of the shake table experiments is based on the *"idealized prototype"* soil profile (Fig. 3**a, b**). Naturally, the seismic response of the *"idealized prototype"* (equivalent single layer) cannot be identical to that of the *prototype* (multi-layered soil profile), but the discrepancies should not exceed 20%, at least for the first natural period (Gazetas, 1982).

The *model soil* should: (a) satisfy the similitude relation of Eq. (4); and (b) have a shear modulus distribution G_0 with depth similar to that of the *idealized prototype*. Comparing to the remodeled soil (Xianfeng et al., 2017), synthetic soil allows more flexibility in terms of adjusting its properties to fit the desired scaling relation. The target stiffness and density (required to satisfy Eq. (4)) can be attained by adjusting the proportions of the components of the mixture. By adding a reduced density component to the mixture, the produced synthetic soil can satisfy similarity (Eq. (4) and G_0 distribution) and also be substantially lighter than the real soil, thus offering the possibility to use a larger geometry scale S_l (given the capacity of the shaking table, a larger model can be tested if the model soil density is reduced). Within this context, a *synthetic model soil* composed of dry sand and sawdust is employed in this study. After laboratory testing, a mass ratio of sand and sawdust of 2.5:1 is finally selected. The "actual" scale factors of the synthetic soil are compared to the "designed" one (Table 2), showing that the synthetic soil satisfies the previously discussed similarity conditions.

To characterize the properties of *synthetic model soil*, a series of resonant column tests are conducted at different confining pressures (20, 50, 100, and 150 kPa). The tests aimed at measuring the small-strain shear modulus G_0, the degradation of the secant shear modulus with shear strain ($G - \gamma$), and the corresponding damping ratio–shear strain ($\xi - \gamma$) relations of the synthetic model soil. Resonant column tests are well-suited for this purpose, as they offer the possibility to test the soil material from small (10^{-5} or less) to relatively large shear strains. As summarized in Table 3, the measured G_0 increases nonlinearly with the confining stress σ_0'. Hardin and Richart (1963) proposed a general relation for G_0 in function of the mean effective stress σ_0':

$$G_0 = a\frac{(2.973 - e)^2}{1 + e}(\sigma_0')^n \tag{5a}$$

where a and n are parameters that depend on the type of soil; and e is the voids ratio. Based on the laboratory results, such a relation is derived for the synthetic model soil:

$$G_0 = 141.4 \times (\sigma_0')^{0.702} \tag{5b}$$

The fitted distribution (Eq. (5b)) of the synthetic model soil is compared in Fig. 3**c** to that of the idealized scaled-down prototype (model scale), confirming its adequate matching.

Fig. 4 compares the measured $G/G_0 - \gamma$ and $\xi - \gamma$ curves of the *synthetic model soil* to the *prototype soil* (mud clay, which is the most representative of the prototype conditions and located near the station) and the published curves of Ishibashi and Zhang (1993). As shown in Fig. 4**a**, the $G/G_0 - \gamma$ curves of the *synthetic model soil* compare well to those of the *prototype soil*. The experimental results also compare well with the published curves of Ishibashi and Zhang (1993) for clay under different confining pressures, and plasticity index $PI = 20$, which is a representative value of the *prototype soil*. As expected for clayey materials, the confining pressure σ_0' has a limited effect on the shape of the $G/G_0 - \gamma$ curves. The same applies to the model soil, despite the fact that it is based on sand. As shown in Fig. 4**b**, the $\xi - \gamma$ curves of the *synthetic model soil* compare well with the *prototype soil* and the published data. There are some discrepancies for the range of strains 10^{-5} to 10^{-4}, where the synthetic soil exhibits slightly higher damping, but overall the comparison is acceptable. It may therefore be concluded that the *synthetic model soil* achieves similar dynamic response with the *prototype soil*, and can therefore be used for the 1 g shaking table tests.

Fig. 5 compares the grain size distribution of the *synthetic model soil* to that of its two constituents (sand and sawdust). The uniformity coefficient and the mean particle size of the utilized sand, sawdust and the resulting synthetic soil are C_u= 1.97, 2.78 and 2.92; and d_{50}= 0.36 mm, 0.23 mm and 0.34 mm, respectively. The key properties of the model soil, obtained from standard laboratory tests are summarized as follows: density ρ= 860 kg/m^3 (D_r = 92%, density at densest and loosest possible stateρ_{max} = 936 kg/m^3, and ρ_{min} = 508 kg/m^3,

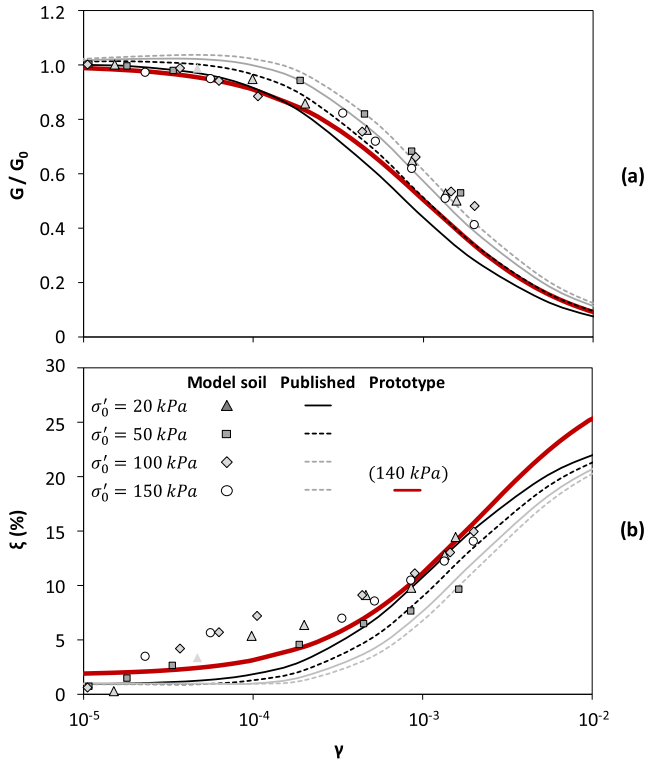

Fig. 4. Comparison of resonant column test results of *prototype* (mud clay, PI = 20) and *synthetic model soil* to the published curves of Ishibashi and Zhang, 1993, for PI = 20: (a) $G/G_0 - \gamma$; (b) $\xi - \gamma$.

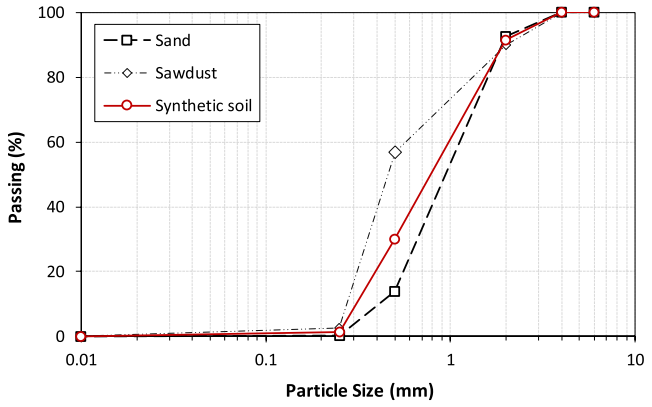

Fig. 5. Grain size distribution of the *synthetic model soil* (2.5:1 mixture of sand and sawdust, based on mass).

respectively); peak friction angle $\varphi = 30.7^{o}$; cohesion c= 1 kPa. The *synthetic model soil* is prepared before the experiments by mixing sand and sawdust using a blender. Before mixing, the sawdust and the sand are dried using an oven. The physical model is constructed layer by layer. Each layer (of 8 cm thickness) is prepared by pouring the *model soil* mixture into the laminar container. The desired density of 860 kg/m^3 is achieved by controlling the weight of the soil of each layer (to prepare one layer of 8 cm thickness, 0.08 × 860 kg/m^3 = 68.8 kg/m^2 are used). Then, a 2 m × 2 m steel plate is used to compact the layer by tamping, until reaching the target thickness (volume). A total of 25 layers were needed to complete the 2 m deep physical model, which is described in the next sections.

2.3. Model structure

The cross-section of the prototype subway station is illustrated in Fig. 1. To model the internal structures (columns, beams, and slabs) in proper detail, granular concrete is adopted as the material of the model structure. The granular concrete (Zhang et al., 2019a) is a mixture of cement, sand, lime, and water, with a ratio by mass of 1:5.8:0.6:0.6, respectively. As shown in Table 4, the compressive strength f'_c of the granular concrete is 10.5 MPa, which allows maintaining similarity in terms of bending moment capacity. Galvanized steel wires are utilized for the longitudinal and transverse reinforcement. The reinforcement ratios are determined by considering the bending moment resistances of the prototype structure, scaled-down employing the previously discussed similitude relations. The dimensions and compressive strength of the steel wires are summarized in Table 4.

Table 4
Properties and key dimensions of materials used to construct the model structure.

	Φ (mm)	ρ (kg/m^3)	Strength (MPa)	E (MPa)
Steel wire 22	0.7	7850	312	205
Steel wire 18	1.2	7850	347	205
Granular concrete	–	1860	10.5	9600

As illustrated in Fig. 6, the construction of the model structure includes three main stages. Initially, the reinforcement cage is prepared and installed in a temporary formwork (Fig. 6**a**). Then, the granular concrete mixture is placed (Fig. 6**b**) and allowed to cure for 28 days before removing the formwork. As shown in Fig. 6**c**, the model structure has a length of 1600 mm, containing 5 rows of dual columns with a column spacing of 364 mm. To avoid boundary effects, the instrumented cross-section is in the middle of the model structure. At the two ends of the model structure, plastic plates are installed to cover the model, so as to avoid the model soil entering into the model structure.

The relative stiffness of the tunnel structure with respect to the surrounding soil is an important aspect. According to Wang (1993), the similitude ratio S_F in terms of flexibility (relative stiffness) can be derived as follows:

$$S_F = \left(\frac{G_m W_m}{S_m H_m}\right) / \left(\frac{G_p W_p}{S_p H_p}\right) = S_G / S_S \tag{6}$$

where the subscripts m and p represent the model and the prototype, respectively; $G$is the shear modulus of soil, W, H, and S are the width, height, and unit stiffness of the structure, respectively. The average elastic shear modulus of the soil near the structure is used to calculate the flexibility ratio for the prototype and the model. The stiffness of the structure, S is calculated by simple frame analysis using the FE method. A flexibility similitude ratio S_F of 1:1.4 is obtained, which implies that the relative stiffness of the model structure is 1.4 times greater than that of the prototype. This discrepancy is difficult to avoid, given the choice of granular concrete as the material of the model structure.

2.4. Instrumentation

The key dimensions (in mm) of the physical model and the instrumentation layout are summarized in Fig. 7. The instrumented section (Fig. 6**c**) includes 10 accelerometers (Setra 141), 2 wire displacement transducers (DP-500F), and 5 earth pressure transducers (CYY9-30). Seven accelerometers (A1-A7) are installed 990 mm away from the model structure, representing the “free-field” array. Three accelerometers (A8-A10) and five earth pressure sensors (P1-P5) are installed on the outer surface of the sidewalls. All sensors are connected to the multi-channel data acquisition system of the shaking table in order to ensure that the signals are fully synchronized. In addition, as discussed later on, 18 strain gauges are also installed to measure the flexural distortion of the underground structure. These were installed during the construction of the model structure, before its installation in the soil.

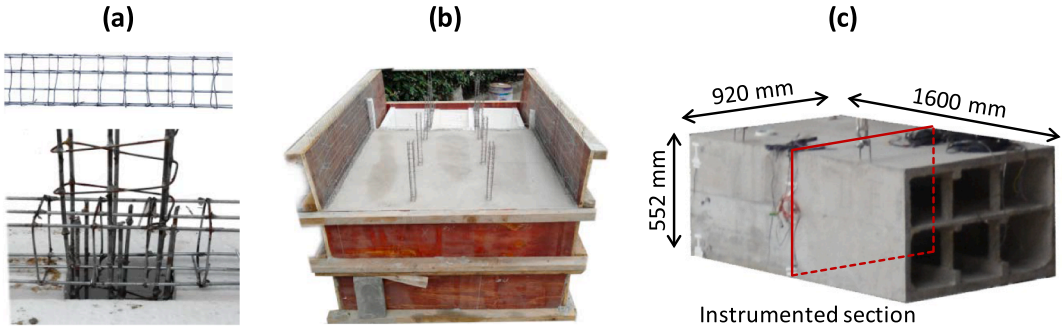

Fig. 6. Construction of model structure: (a) preparation of reinforcement cage; (b) concrete casting in a formwork; and (c) final model structure after curing and removal of formwork.

2.5. Seismic excitation sequences

The seismic input motion is imposed in the transverse direction x of the station (Fig. 7). As summarized in Table 5, three series of tests were conducted, employing three successive strong motion sequences. In the first series, the model was subjected to artificial seismic motions, including 10-cycle "sin sweeps" of PGA = 0.1 g of different dominant frequencies, followed by an artificially synthesized Shanghai ground motion (representative for the construction site). The dominant frequencies of the sin sweeps were selected 2 Hz, 4 Hz, 8 Hz, and 10 Hz. In the second series, 4 real records from the PEER Strong Motion Database (Ranf et al., 2001) were applied to the model. The records were selected from sites having similar shear wave velocity ($v_{s,30}$) of the upper 30 m of depth with the prototype site, with the aim of matching the elastic design response spectra on average. In the third series, the Shanghai synthetic ground motion with PGA of 0.2 g and 0.4 g was used as seismic excitation. The seismic excitations are illustrated in Fig. 8, along with their elastic response spectra.

3. Results of shaking table tests

This section summarizes some of the results of the conducted shaking table tests. The discussion focuses on dynamic settlements at the ground surface, strains of the instrumented tunnel cross-section, and dynamic earth pressures. Accelerations are discussed in the next section, in direct comparison with the numerical (FE) prediction.

Table 5
Information and input sequence of earthquake motions.

No.	Earthquake – station	Year	PGA* (g)	$D_{a5\text{-}95}$** (sec)
1	Sin-2 Hz	–	- (0.1)	3.45
2	Sin-4 Hz	–	- (0.1)	1.54
3	Sin-8 Hz	–	- (0.1)	0.81
4	Sin-10 Hz	–	- (0.1)	0.49
5	Shanghai synthetic motion	–	- (0.1)	12.6
6	Kobe – Sakai	1995	0.26 (0.1)	60.1
7	ChiChi – CHY101	1999	0.67 (0.1)	30.4
8	El Mayor Cucapah – Chihuahua	2010	0.42 (0.1)	51.2
9	Darfield – Christchurch Resthaven	2010	0.40 (0.1)	30.5
10	Shanghai synthetic motion	–	- (0.2)	12.6
11	Shanghai synthetic motion	–	- (0.4)	12.6

* PGA of original record (PGA of input motions in the model).
** Significant duration between 5 and 95% of Arias intensity.

3.1. Surface settlements

The time histories of surface settlements at two characteristic locations (L1 above the tunnel centerline, and L2 at a distance) are plotted in Fig. 9. Three characteristic stages of response can be distinguished, being a function of the seismic excitation. During the first stage, which includes the 4 sin sweeps of 0.1 g, practically no settlement is accumulated. The second stage includes the Shanghai synthetic motion and the sequence of 4 real seismic records (Table 5), all scaled

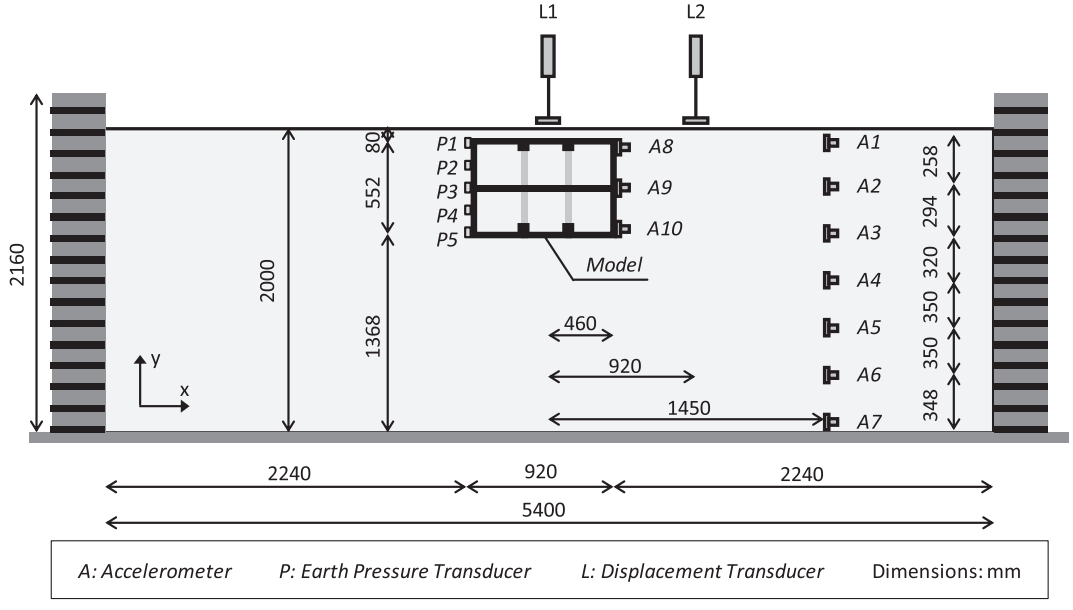

Fig. 7. Shaking table model layout: key dimensions and instrumentation (tunnel strain gauging not shown).

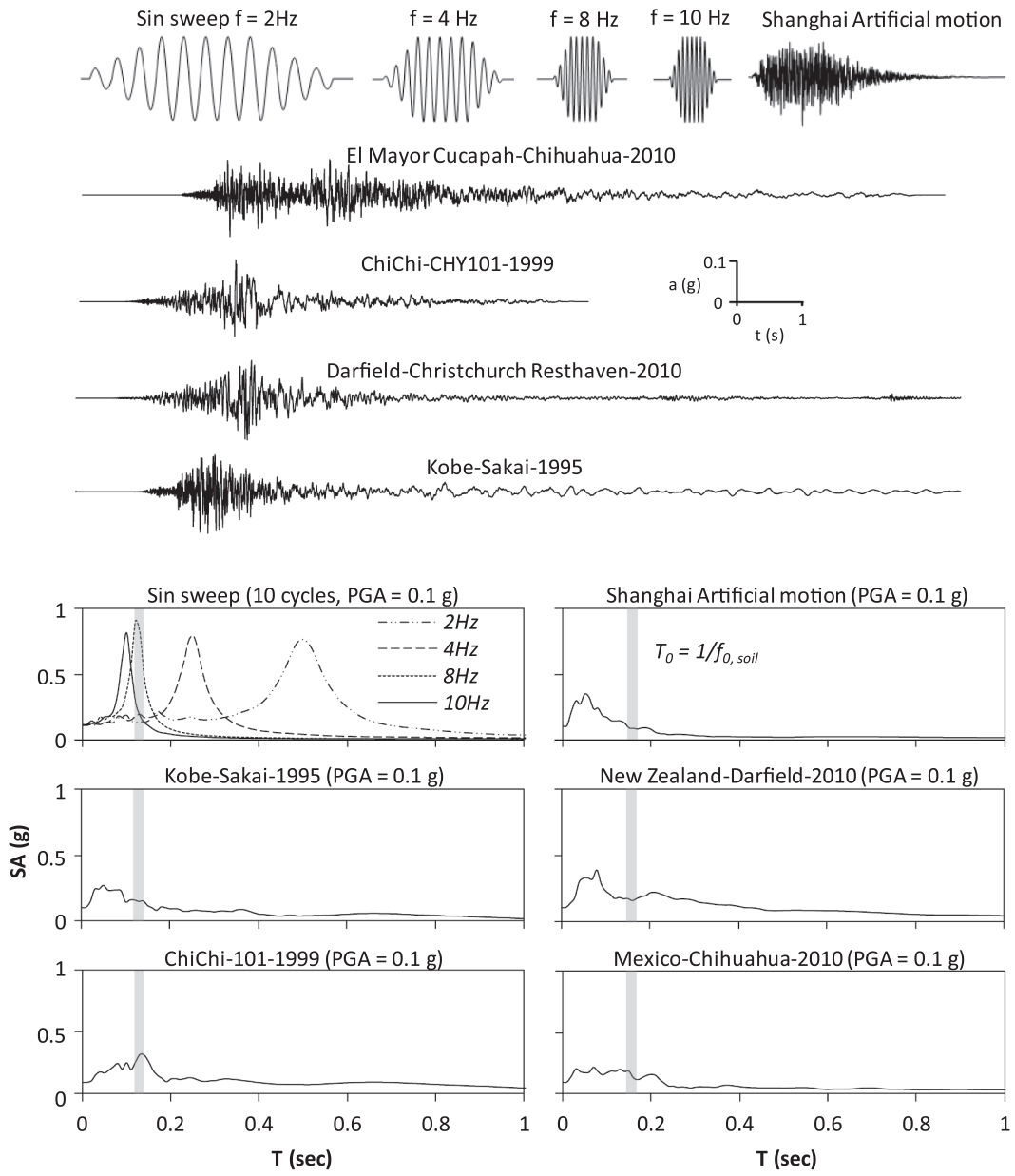

Fig. 8. Seismic excitations used in the shaking table tests, along with their elastic response spectra.

at 0.1 g. Although the PGA is exactly the same with the preceding sin sweeps, a gradual settlement accumulation is observed in the second stages. This large difference can be attributed to the much higher significant duration D_{a5-95} (between 5 and 95% of Arias intensity) of the real records. The third stage refers to the Shanghai synthetic motion, scaled up at 0.2 g and 0.4 g, during which the accumulation of settlement is larger due to the increased acceleration. Comparing the accumulated settlement at the end of shaking, it may be concluded that the presence of the tunnel (under P1) leads to reduction of dynamic settlements (compared to L2), an observation which is consistent with centrifuge test results of the literature (Abuhajar et al., 2015; Pitilakis and Tsinidis, 2014). The settlements above the tunnel (L1) are mainly related to dynamic densification of the soil below the foundation level, and are thus smaller than those recorded at a distance (L2).

3.2. Dynamic strain distribution

The internal beam-column frame is a key difference of the Shanghai metro station to a typical box-type tunnel. According to an early reconnaissance after the 1995 Kobe earthquake (IIDA et al., 1996), more than 20 intermediate columns of the Dakai Station failed completely, resulting to the collapse of the entire station and the consequent 2.5 m subsidence of the road above the station. Several studies (e.g., Shawky and Maekawa, 1996) have suggested that the RC columns failed in shear, being a direct result of the racking deformation of the tunnel. Recent dynamic time-history analyses (Lu and Hwang, 2019) indicate that the accumulation of racking deformations led to progressive loss of the vertical bearing capacity of the internal columns, with failure being initiated at their base.

In the shaking table tests of this study, strain gauges were installed on critical structural members (internal columns, sidewalls, and slabs), on the upper and lower floor of the model. The peak tensile strains recorded (denoted as positive) under three seismic motions are summarized in Fig. 10. For every measuring location, the recorded peak strain ε_p is normalized to the maximum strain ε_{max} recorded (across the structure) during the same seismic excitation. The maximum tensile

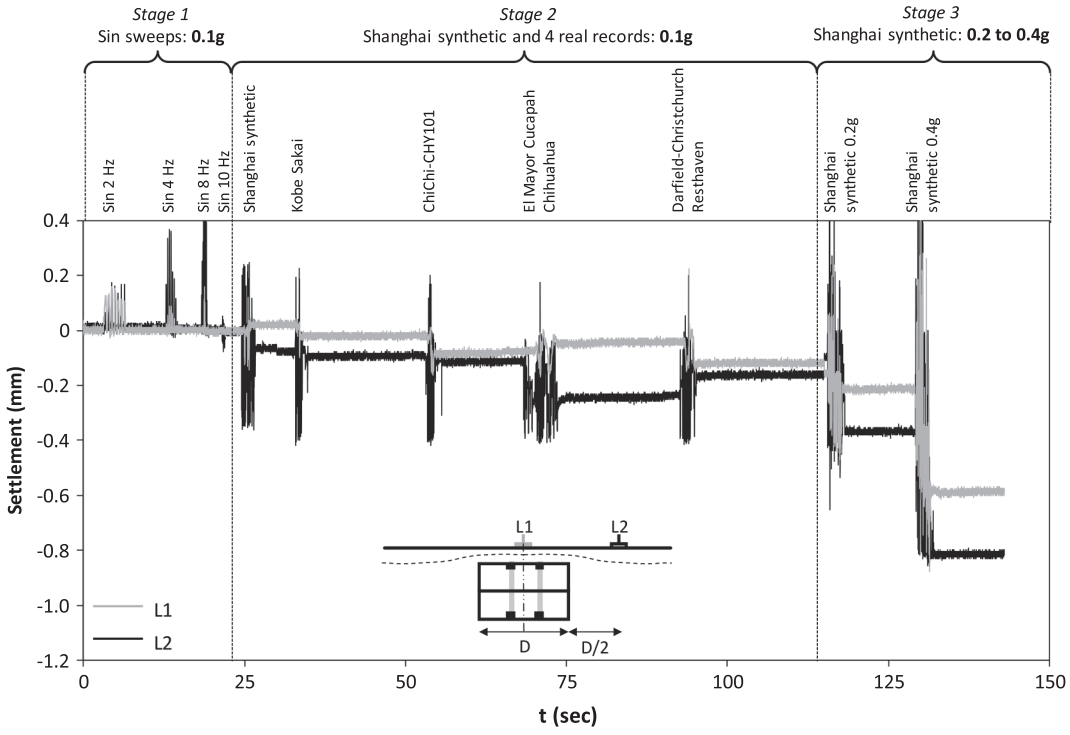

Fig. 9. Time history of experimentally measured ground surface settlements at two characteristic points.

strain is recorded at the base of the lower floor RC columns, which is consistent with the previously discussed collapse initiation of the Daikai metro station. It should be noted that the recorded strain is due to combined bending and axial loading. Before seismic shaking, the maximum strain (and hence stress) is observed at the base of the lower floor columns and sidewalls, being the result of the self-weight of the metro station and of the overburden soil. The initial higher axial loading leads to larger compression ratio of the lower floor RC columns, which leads to an increase of their bending moment capacity but also to a decrease of their ductility. In the absence of proper reinforcement detailing, the base of the lower floor columns could be prone to seismic failure, as was the case for the Daikai metro station. The top of upper and lower floor RC columns comes second in terms of tensile strains, while the sidewalls and the slabs sustain much smaller strains due to

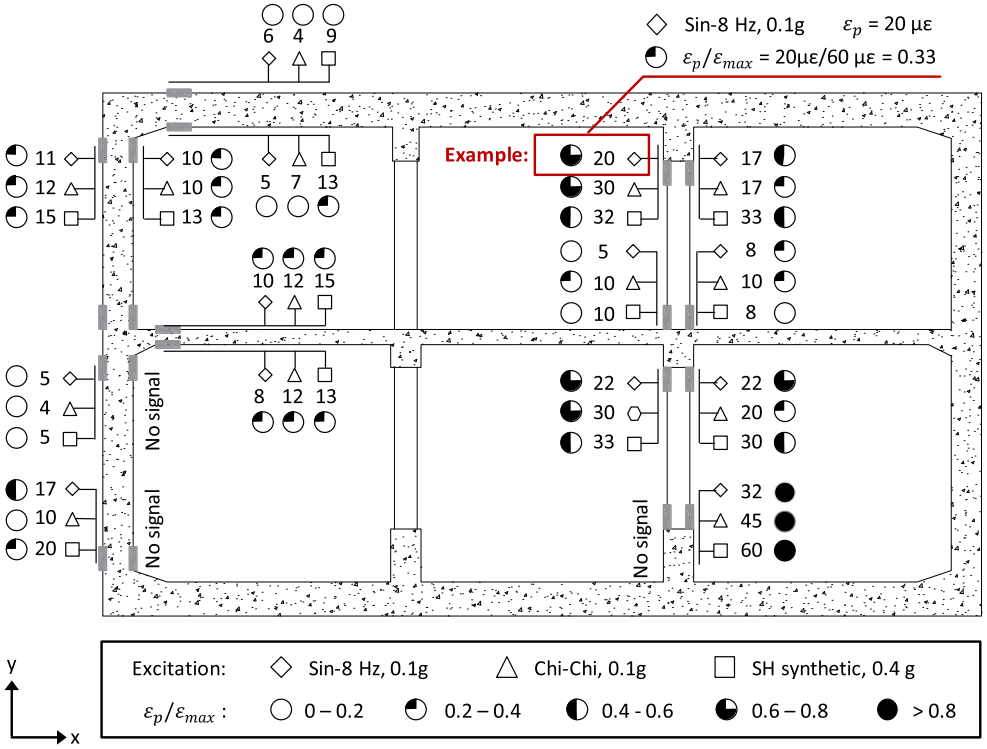

Fig. 10. Ratio of peak strain ε_p normalized to the maximum strain ε_{max} recorded (across the structure) during the same excitation. In addition to $\varepsilon_p/\varepsilon_{max}$, the absolute value of ε_p (με) is also shown.

their significantly larger stiffness.

Selected time histories of strain pairs of different structural components are compared in Fig. 11. The locations of the various strain gauges are shown in Fig. 11**a**, along with a snapshot (t = 2.73 sec) showing the (hypothesized) racking deformation of the station. The pairs of tensile and compressive strains that correspond to the selected snapshot are visualized in the strain time histories of Fig. 11**b**. Although the strains were recorded only at specific locations, the recorded strain distribution fits well the hypothesis of racking deformation. In the absence of displacement measurements, the rocking mode of response (Zhao et al., 2019) cannot be reliably quantified. An estimation is possible on the basis of acceleration measurements, but the results are sensitive to double integration errors.

3.3. Dynamic earth pressures

An example of recorded earth pressure time histories (dynamic part) at two characteristic locations (P3 and P5) on the sidewall of the metro station are depicted in Fig. 12. The dynamic earth pressure recorded near the bottom slab (P5) is larger than the one close to the middle floor slab (P3). Among the 0.1 g sin-sweeps (Stage 1), the maximum dynamic earth pressure is observed for the one having 8 Hz dominant frequency. From the 0.1 g real seismic motions (Stage 2), Chi-Chi was the one to produce the highest dynamic earth pressures. In both cases, this is most probably due to the proximity of the dominant frequency of the seismic motions to that of the model soil. Interestingly, the 0.4 g Shanghai synthetic motion did not only produce the largest dynamic earth pressures, but also led to their permanent (post-seismic) increase: 0.15 kPa at P5 (base) and 0.04 kPa at P3 (middle).

4. Numerical analysis of shaking table tests

In this section, the shaking table tests are simulated with nonlinear finite elements (FE), assuming the properties of the synthetic soil. The experimental results are used as a benchmark in order to validate the numerical analysis method. In the next section, the validated FE modelling technique is used to analyze the seismic response of the prototype.

4.1. Numerical modelling

The problem is analyzed under plane-strain conditions, employing the FE code ABAQUS (Hibbitt et al., 2012). As shown in Fig. 13**a**, the soil is modelled with quadrilateral continuum elements, using a modified kinematic hardening constitutive model to capture nonlinear soil response (Fig. 13**b**). The metro station (assumed elastic) is modelled with beam elements. An equivalent “slice” of the structure is analyzed, accounting for column spacing in the out-of-plane direction. The soil-tunnel interface is modelled with special contact elements, allowing for slippage and separation. Based on interface tests, an interface friction angle of $\delta = 11.5^{\circ}$ is assumed and a sensitivity analysis is conducted to address potential uncertainties. The lateral model boundaries are connected with appropriate kinematic constraints, mimicking the laminar box (each node at one side of the model is rigidly connected to the corresponding node at the same elevation on the opposite side). The adopted boundary has been shown to offer good results (e.g., Tsinidis

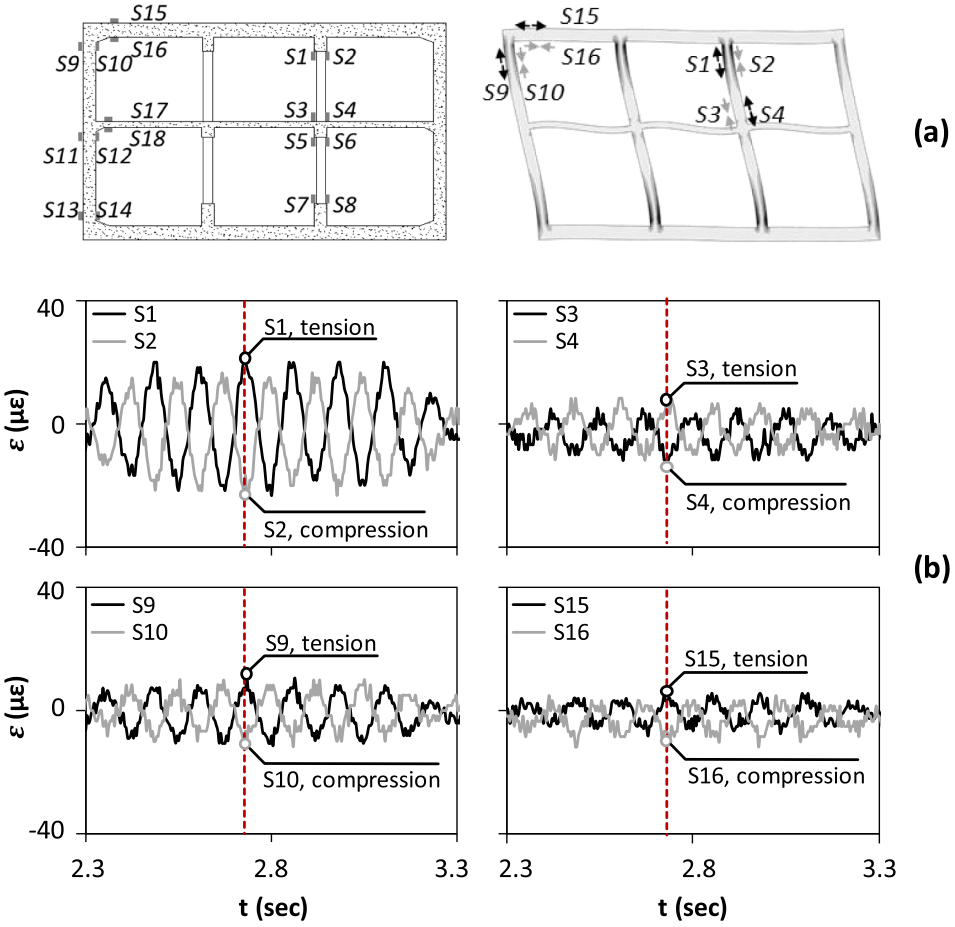

Fig. 11. Strain measurements for Sin-8 Hz, 0.1 g excitation: (a) layout of strain gauges on the tunnel model, and snapshot (t = 2.73 sec) showing the (hypothesized) racking deformation of the metro station; and (b) time histories of dynamic strains on upper floor column (S1–S4), side wall (S9–S10), and the top slab (S15–S16).

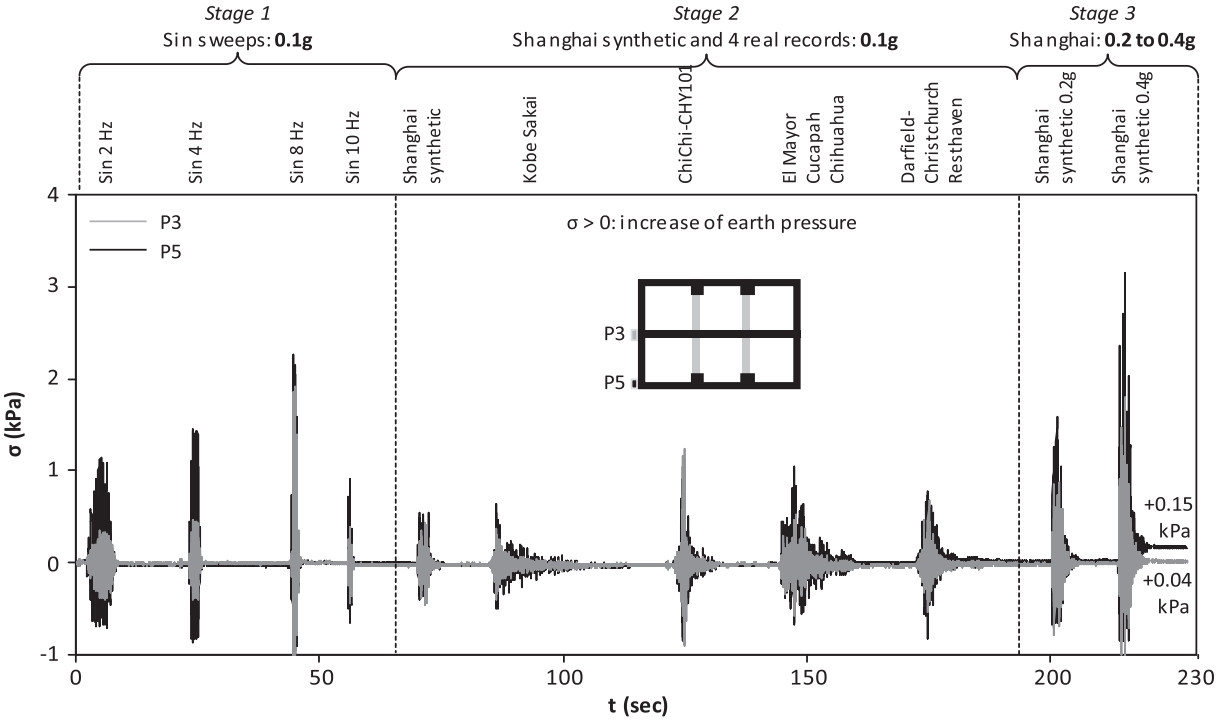

Fig. 12. Dynamic earth pressure time histories recorded at two characteristic locations on the metro station sidewall: P3 at the middle slab; and P5 at the bottom slab.

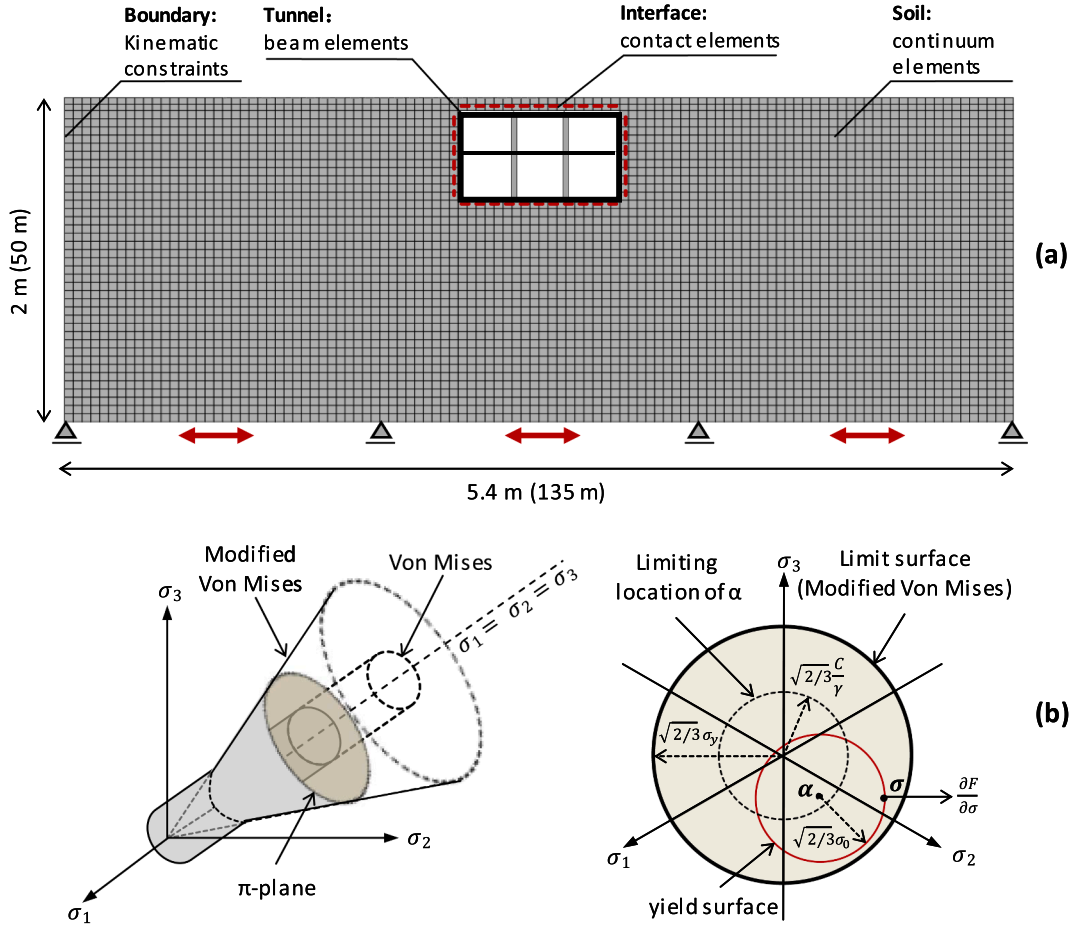

Fig. 13. Finite element modelling: (a) model overview, prototype dimension shows in brackets; and (b) representation of the extended Von Mises failure criterion in the principal stress space (left) and of the failure surface on the π-plane (right) (Anastasopoulos et al., 2011).

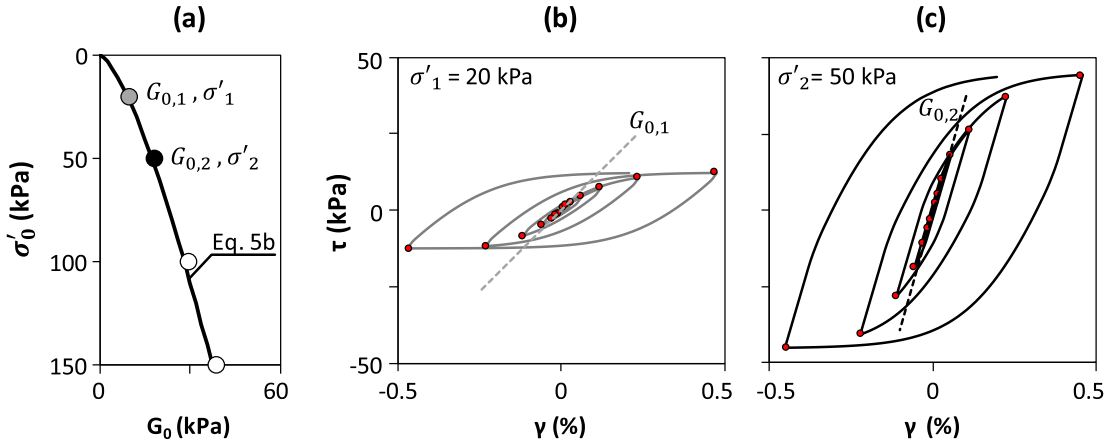

Fig. 14. Model calibration for synthetic model soil: (a) small-strain shear modulus G_0 in function of confining pressure σ'_0 (calibrated FE model vs. Eq. (5b)); shear stress–shear strain ($\tau - \gamma$) response of the calibrated FE model for two confining pressures: (b) 20 kPa; and (c) 50 kPa.

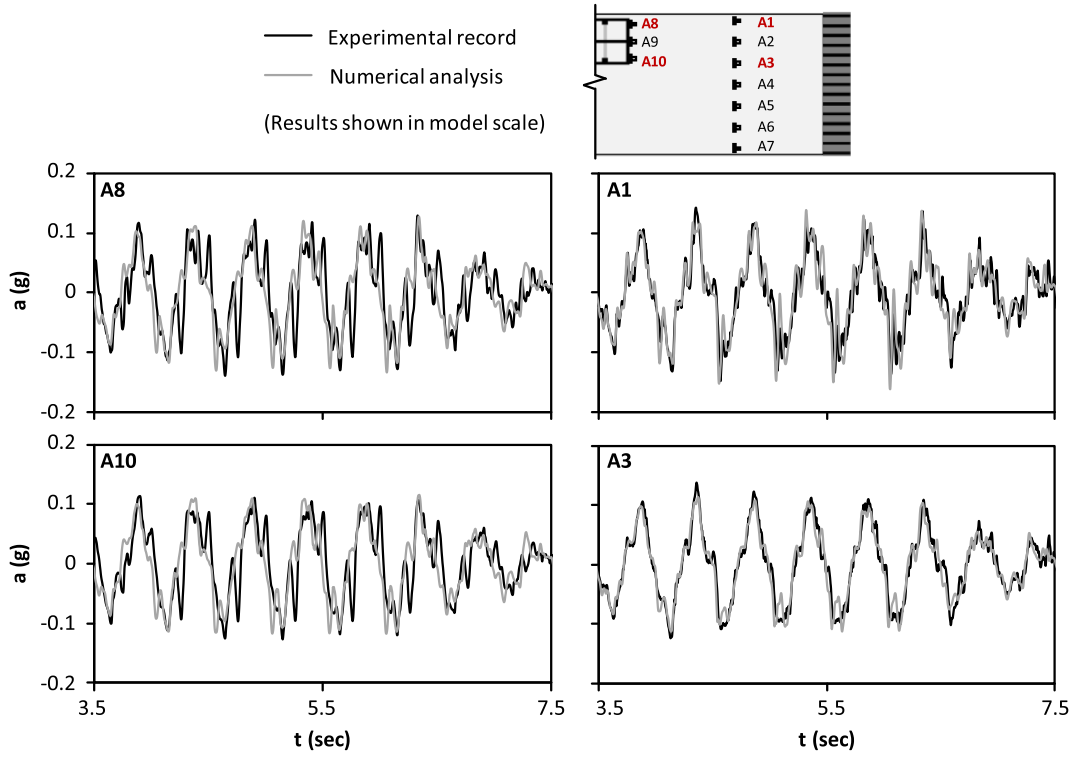

Fig. 15. Comparison of numerical prediction to recorded acceleration time histories at representative locations on the tunnel (A8 and A10) and at a distance (A1 and A3), for sin sweep f= 2 Hz seismic excitation.

et al., 2014), provided that the distance of the tunnel to the lateral boundary is adequately large. The analysis is conducted in two steps: (1) static application of the geostatic stresses; and (2) dynamic time history analysis, imposing the seismic motions at the base of the model. To model the shaking table tests as accurately as possible, the acceleration time histories recorded by accelerometer A7 (attached on the shaking table, see Fig. 7) are used as seismic excitation.

Nonlinear soil response is modelled through a modified kinematic hardening constitutive model, combining an extended pressure-dependent Von Mises failure criterion and associated flow rule (Anastasopoulos et al., 2011). The model is an extension of the *pressure-independent* model of Lemaitre and Chaboche (1990), which is based on the work of Armstrong and Frederick (1966). The extended *pressure-dependent* model is encoded in ABAQUS through a user subroutine. The evolution of stresses is defined as:

$$\sigma = \sigma_0 + \alpha \tag{7}$$

where σ_0 is the yield stress and α describes the kinematic evolution of the yield surface in the stress space, called “backstress”. The yield surface is described by a function:

$$F = f(\sigma - \alpha) - \sigma_0 \tag{8}$$

where $f(\sigma - \alpha)$ is the equivalent Mises stress in relation to the backstress α. According to the associated plastic flow rule, the rate of plastic flow $\dot{\varepsilon}^{pl}$ is:

$$\dot{\varepsilon}^{pl} = \dot{\bar{\varepsilon}}^{pl}\frac{\partial F}{\partial \sigma} \tag{9}$$

where $\dot{\bar{\varepsilon}}^{pl}$ is the equivalent plastic strain rate, defined as:

$$\dot{\bar{\varepsilon}}^{pl} = \sqrt{\frac{2}{3}\dot{\varepsilon}^{pl} : \dot{\varepsilon}^{pl}} \tag{10}$$

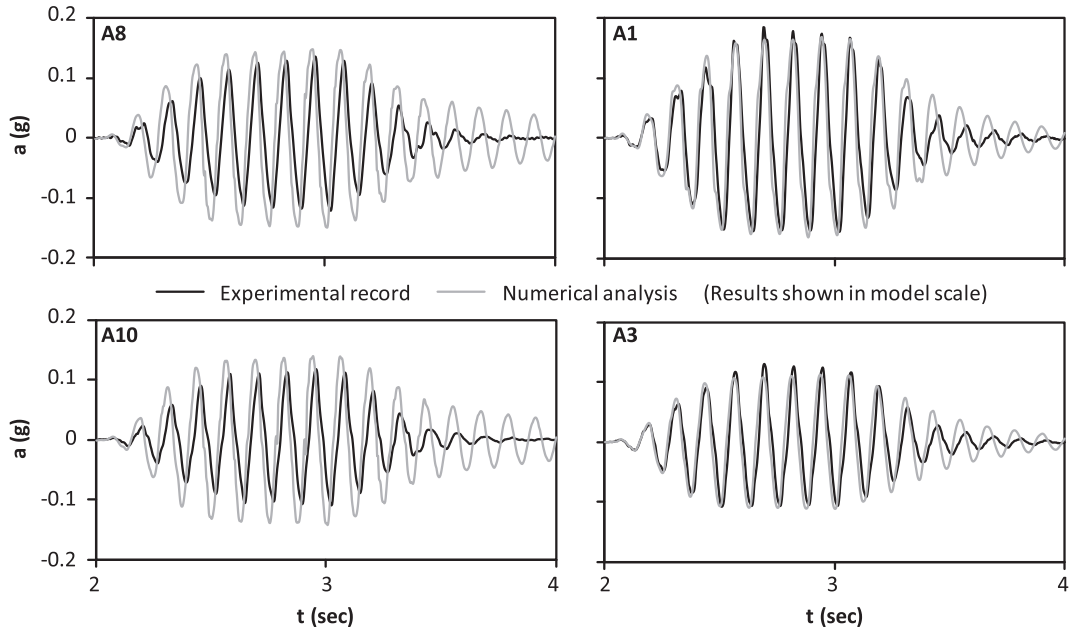

Fig. 16. Comparison of numerical prediction to recorded acceleration time histories at representative locations on the tunnel (A8 and A10) and at a distance (A1 and A3), for sin sweep $f = 8$ Hz seismic excitation.

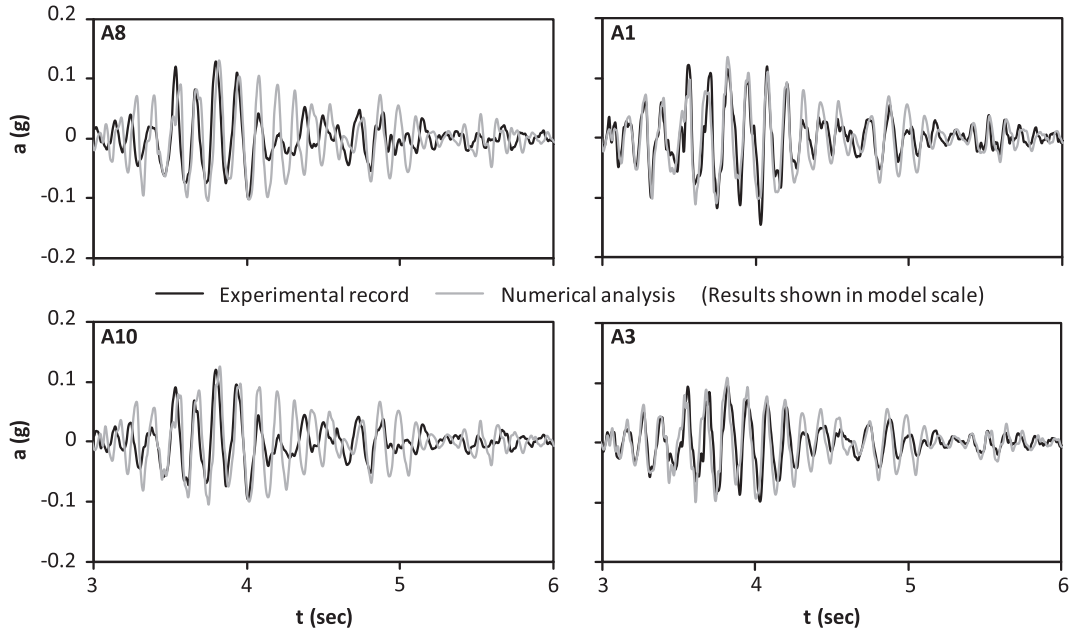

Fig. 17. Comparison of numerical prediction to recorded acceleration time histories at representative locations on the tunnel (A8 and A10) and at a distance (A1 and A3), for Chi-Chi seismic excitation.

The kinematic hardening rule for the backstress contains a "recall" term, which incorporates the fading memory effect of the strain path:

$$\dot{\alpha} = C\frac{1}{\sigma_0}(\sigma - \alpha)\dot{\varepsilon}^{pl} - \gamma_k \alpha \dot{\varepsilon}^{pl} \tag{11}$$

where $C = E = 2(1 + \upsilon)$ is the initial kinematic hardening modulus; and γ_k determines the rate of decrease of the kinematic hardening modulus with increasing plastic strain. The previously mentioned "recall" term is introduced by the term $\gamma_k \alpha \dot{\varepsilon}^{pl}$.

Fig. 13**b** illustrates a representation of the model in the principal stress space (left), and of the failure surface on the π-plane (right). The kinematic hardening rule implies that the backstress α is contained within a cylinder of radius $\sqrt{2/3}\alpha^s$ $(=\sqrt{2/3}C/\gamma_k)$, where α^s is the magnitude of α at large plastic strains. Since the yield surface remains inside the limit surface, it also implies that any stress point must lie within a cylinder of radius $\sqrt{2/3}\sigma_y$, where σ_y is the maximum yield stress at large plastic strains, and therefore:

$$\frac{C}{\gamma_k} = \alpha_s = \sigma_y - \sigma_0 \tag{12}$$

In the case of clays, the undrained shear strength S_u is pressure independent and the maximum yield stress can be defined as:

$$\sigma_y = \sqrt{3}S_u \tag{13}$$

Given that $\sigma_y = C/\gamma + \sigma_0$, parameter γ can be expressed as (Gerolymos et al., 2005):

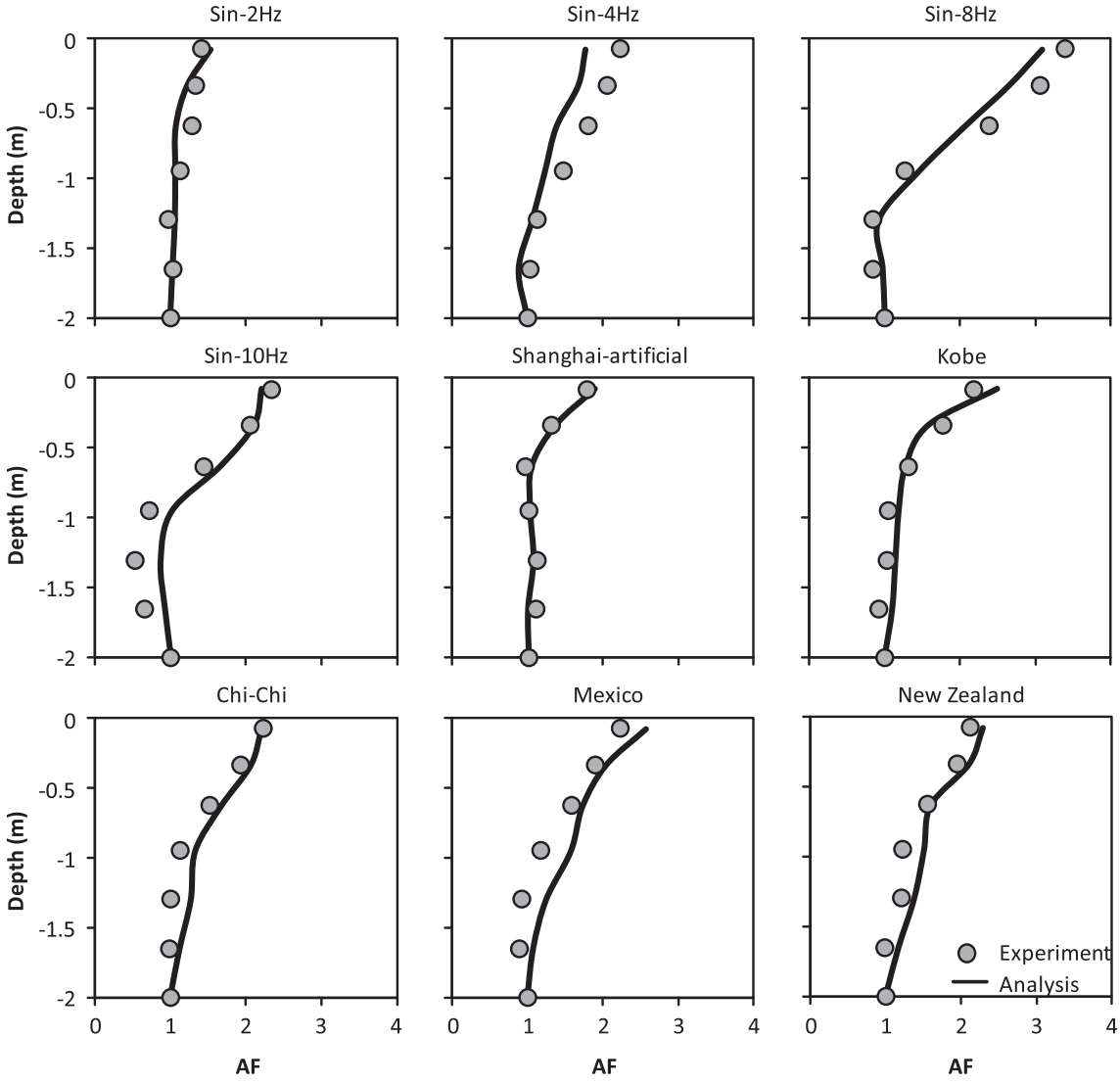

Fig. 18. Comparison of numerically predicted to recorded maximum horizontal acceleration amplification factors (*AF*) at a distance from the tunnel (A1-A7) in function of depth, for all 0.1 g seismic excitations.

$$\gamma_k = \frac{C}{\sqrt{3}S_u} \tag{14}$$

In the case of cohesionless (sandy) soil, the shear strength depends on the *confining pressure* and the friction angle φ. The pressure dependency is brought in by defining the yield stress σ_y as a function of octahedral stress and the friction angle:

$$\sigma_y = \sqrt{3}\left(\frac{\sigma_1 + \sigma_2 + \sigma_3}{3}\right) sin\varphi \tag{15}$$

where σ_1, σ_2, and σ_3 represent the principal stresses. The parameter γ can be expressed as:

$$\gamma_k = \frac{C}{\sqrt{3}\left(\frac{\sigma_1 + \sigma_2 + \sigma_3}{3}\right) sin\varphi} \tag{16}$$

Parameter σ_0, which defines the yield stress at zero plastic strain (i.e., the initiation of the nonlinear regime), is defined as a fraction λ_0 of the yield stress σ_y.

A key advantage of such simplified model is it's straight-forward calibration, which only requires: (a) shear strength: S_u for clay, φ for sand; (2) small-strain stiffness: G_0or V_s; and (3) $G - \gamma$ curves (λ_0). The model has been validated for shallow foundations (Anastasopoulos et al., 2011), using as benchmark centrifuge tests conducted at UC Davis (Kutter et al., 2003) and TRISEE large scale tests (Faccioli et al., 1999). It was later validated for a variety of soil-structure systems, including pile foundations (Giannakos et al., 2012) and tunnels (Tsinidis et al., 2014). The latter is an independent validation, forming part of a numerical round robin on centrifuge model tests conducted at the University of Cambridge (Lanzano et al., 2015). The *pressure-dependent* kinematic hardening model achieved very good predictions, in many cases outperforming more sophisticated constitutive models (Bilotta et al., 2014).

4.2. Calibration for synthetic model soil

The constitutive model is calibrated for the synthetic model soil using the results of previously discussed resonant column and direct shear tests. The measured properties of the synthetic model soil are adopted: ρ= 860 kg/m^3 (D_r = 0.92); φ = 30.7°; and c= 1 kPa. With respect to the small-strain shear modulus, the derived relation (Eq. (5b)) is adopted, which is based on the expression of Hardin and Richart (1963) and the measured data of Table 3. Fig. 14**a** compares the calibrated model (dots) to Eq. (5b) (line). As shown in Fig. 4, the $G - \gamma$, $\xi - \gamma$ curves of the synthetic model soil are insensitive to the confining pressure. Therefore, the average of the four $G - \gamma$, $\xi - \gamma$ curves of Fig. 4 is used for model calibration. The shear stress–shear strain ($\tau - \gamma$)

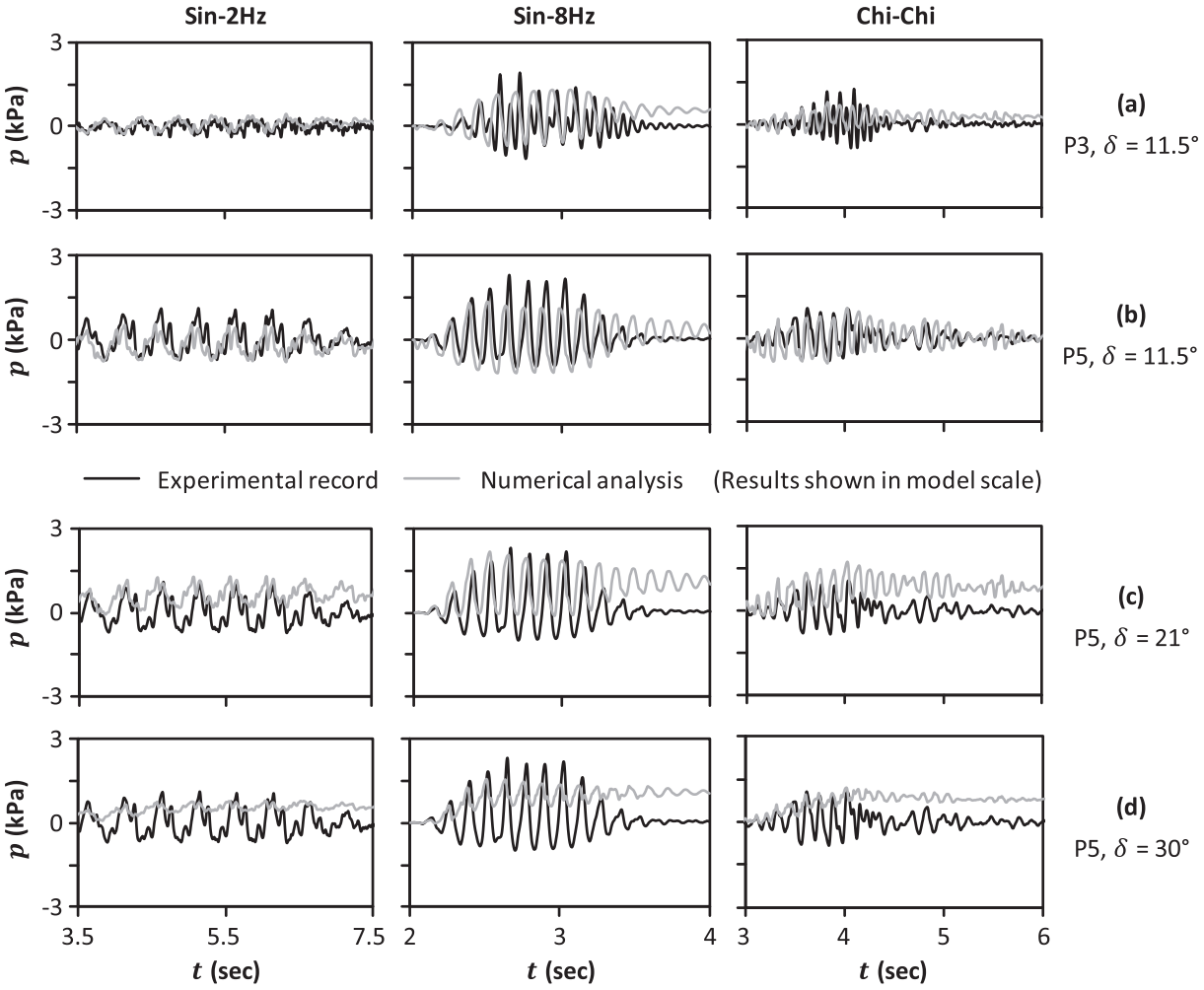

Fig. 19. Comparison of numerically predicted to recorded time histories of dynamic earth pressures p at different elevations, varying the friction angle δ of the soil-structure interface: (a) P3, at the middle of the structure, δ = 11. 5°; (b) P5, at the bottom of the structure, δ = 11. 5°; (c) P5, δ = 21°; and (d) P5, δ = 30°.

response of the calibrated model is shown in Fig. 14**b, c** for two different confining pressures (20 kPa and 50 kPa).

4.3. Analysis vs. 1 g shaking table test

The calibrated model is used to simulate the 1 g shaking table tests. In this section, some representative comparisons are made in terms of accelerations and soil pressures. A selection of numerically predicted acceleration time histories is compared to the experimental measurements for three representative seismic excitations: sin sweep f= 2 Hz (Fig. 15), sin sweep f= 8 Hz (Fig. 16), and Chi-Chi-CHY101 (Fig. 17).

The numerical predictions compare well with the recorded data for all seismic excitations (also for the ones not shown herein). However, after the main strong motion cycles, the numerically predicted acceleration decreases slower than the recorded one for the higher frequency f= 8 Hz sin sweep (Fig. 16) and the Chi-Chi seismic excitation (Fig. 17), while the discrepancies are negligible for the lower frequency f= 2 Hz sin sweep (Fig. 15). This may be attributed to differences in small-strain damping, which may also be related to additional damping by the laminar box (which is assumed zero in the analysis).

Fig. 18 compares the numerically predicted to the recorded maximum horizontal acceleration amplification factors (AF) at a distance from the tunnel (sensors A1-A7) in function of depth, for all 0.1 g seismic excitations (all results are shown in model scale). The numerically predicted amplification factors are in good agreement with the experimental results. The largest AF of the order of 3 is observed for the f= 8 Hz sin sweep, which is the one closest to the natural frequency of the model (see also Fig. 8).

Representative comparisons of numerically predicted to experimentally measured dynamic earth pressure time histories at the middle and bottom elevation of the sidewall are presented in Fig. 19**a, b**, assuming interface friction angle δ= 11.5°. Overall, the comparison between analysis and experiment is not bad, but there are certainly some non-negligible discrepancies. In all cases examined, the numerical analysis overestimates the residual earth pressures after the end of shaking, which may be attributed to the associative flow rule of the kinematic hardening constitutive model. The differences in response may be due to a number of factors, in addition to the constitutive model. A first potential factor is the friction angle δ of the soil-structure interface. Although the assumed δ = 11. 5° is based on preliminary interface tests, its effect is explored parametrically by varying it from 11.5° to 21°, and 30° (i.e., 0.38φ, 0.67φ, and 1.00φ). The results of the parametric study are shown for the bottom of the sidewall (P5) in Fig. 19**c, d**. The results confirm the original hypothesis of δ = 11. 5°, as the discrepancies become larger for δ = 21° and 30°. A second potential factor is the measurement accuracy. Soil arching around the pressure sensor may lead to non-uniform contact pressures, increasing the measurement errors (Labuz and Theroux, 2005). In this context, the prediction with δ = 11. 5° is considered acceptable.

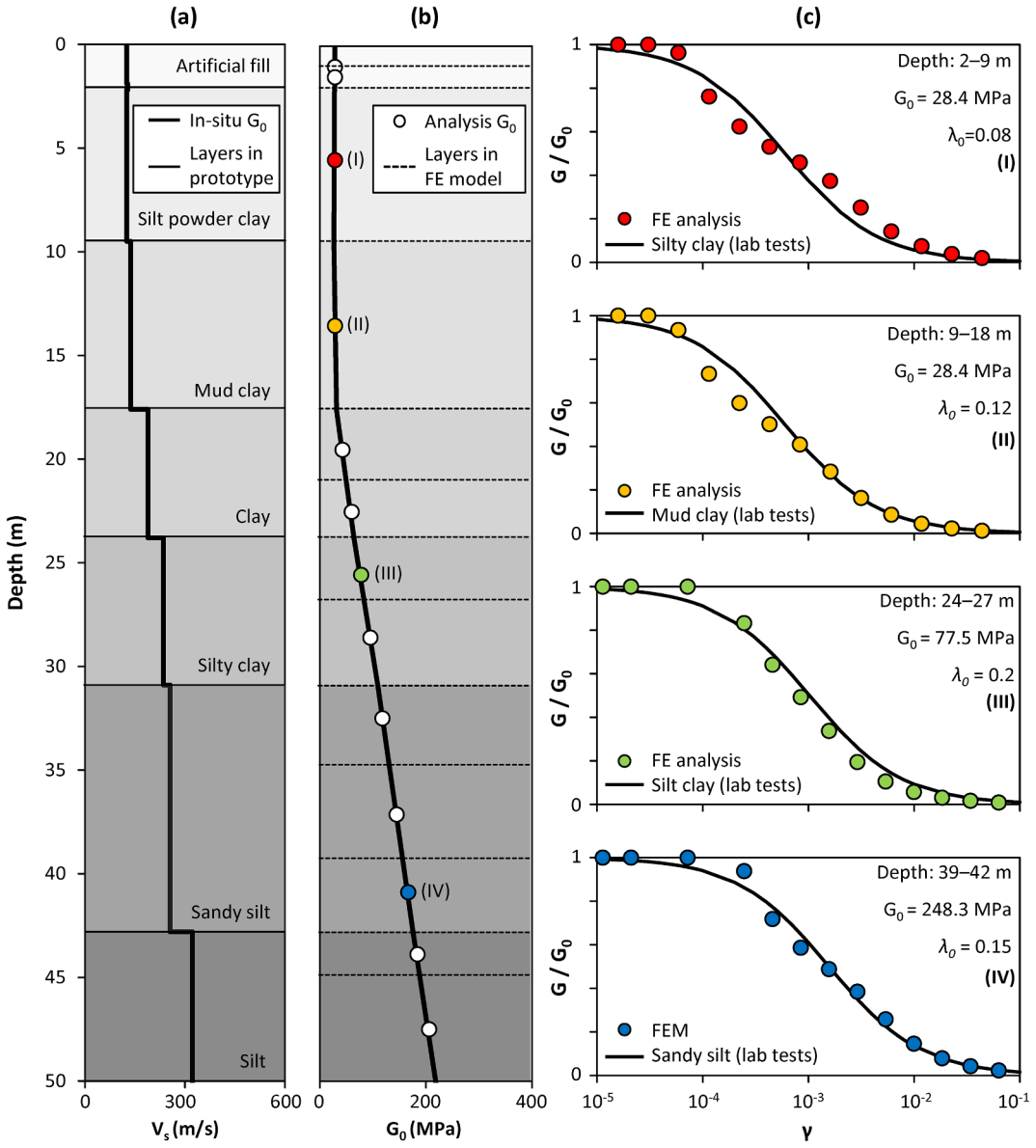

Fig. 20. From model to prototype: (a) prototype multi-layered soil profile and distribution of V_s with depth (based on in-situ down-hole tests); (b) distribution of G_0 with depth based on in-situ V_s measurements compared to FE analysis; and (c) model calibration against measured $G-\gamma$ curves of the prototype layered soil.

5. Numerical prediction of the prototype

In the previous section, the FE modelling technique was validated using the 1 g shaking table tests as benchmark. In this section, the validated model is used to predict the seismic response of the subway station in prototype scale. In this way, the unavoidable challenge of scale effects is indirectly addressed. The prototype-scale results are compared to those corresponding to model-scale, providing quantifiable insights on scale effects. As previously discussed, the *prototype* multi-layered soil profile was simplified to an equivalent single-layer *idealized prototype*, which was materialized by the model soil (mixture of sand and sawdust). Therefore, going from the model "*back to reality*" requires two steps: (1) from *model-scale* to the *idealized prototype*; and (2) from *idealized prototype* to the real *prototype*. The former adapts single layer with stress-dependent (Fig. 3**c**) and non-linear $G/G_0-\xi-\gamma$ (Fig. 4) properties. The latter requires analysis of the multi-layered soil profile of the studied Shanghai Metro Station (Fig. 20). For this purpose, the measured (in-situ down-hole tests) shear wave velocity v_s profile (Fig. 20**a**) and the corresponding small-strain shear modulus G_0 profile (Fig. 20**b**), are used to calibrate the kinematic hardening model for each layer of the prototype soil profile. Examples of such calibration against measured (resonant column tests) $G/G_0-\gamma$ curves are shown in Fig. 20**c**.

As previously discussed, the model of the structure was constructed using granular concrete and steel wires, which allows modelling the structural details of the metro station, including the internal structure. Despite using model soil in order to maintain similarity in the best possible manner (given the challenges of 1 g modelling), the relative stiffness of the structure compared to the surrounding soil was 1.4 times greater in the shaking table *model* compared to the *prototype* (similitude ratio S_F= 1:1.4). In order to be able to isolate the role of scale-effects due to the soil, the stiffness ratio of the *idealized prototype* is maintained equal to that of the *model* (i.e., 1.4 stiffer than reality). This is "brought back to reality" in the analysis of the *prototype*. A second difference between the *idealized prototype* and the *prototype* is the interface friction angle δ. In contrast to the experiments (where the structure was pre-cast), in reality the metro station is cast-in-place. It is therefore more realistic to assume a rough soil-structure interface, setting $\delta=\varphi=30^{\circ}$. In the *idealized prototype*, the interface friction angle is maintained equal to that of that of the *model* ($\delta=11.2^{\circ}$).

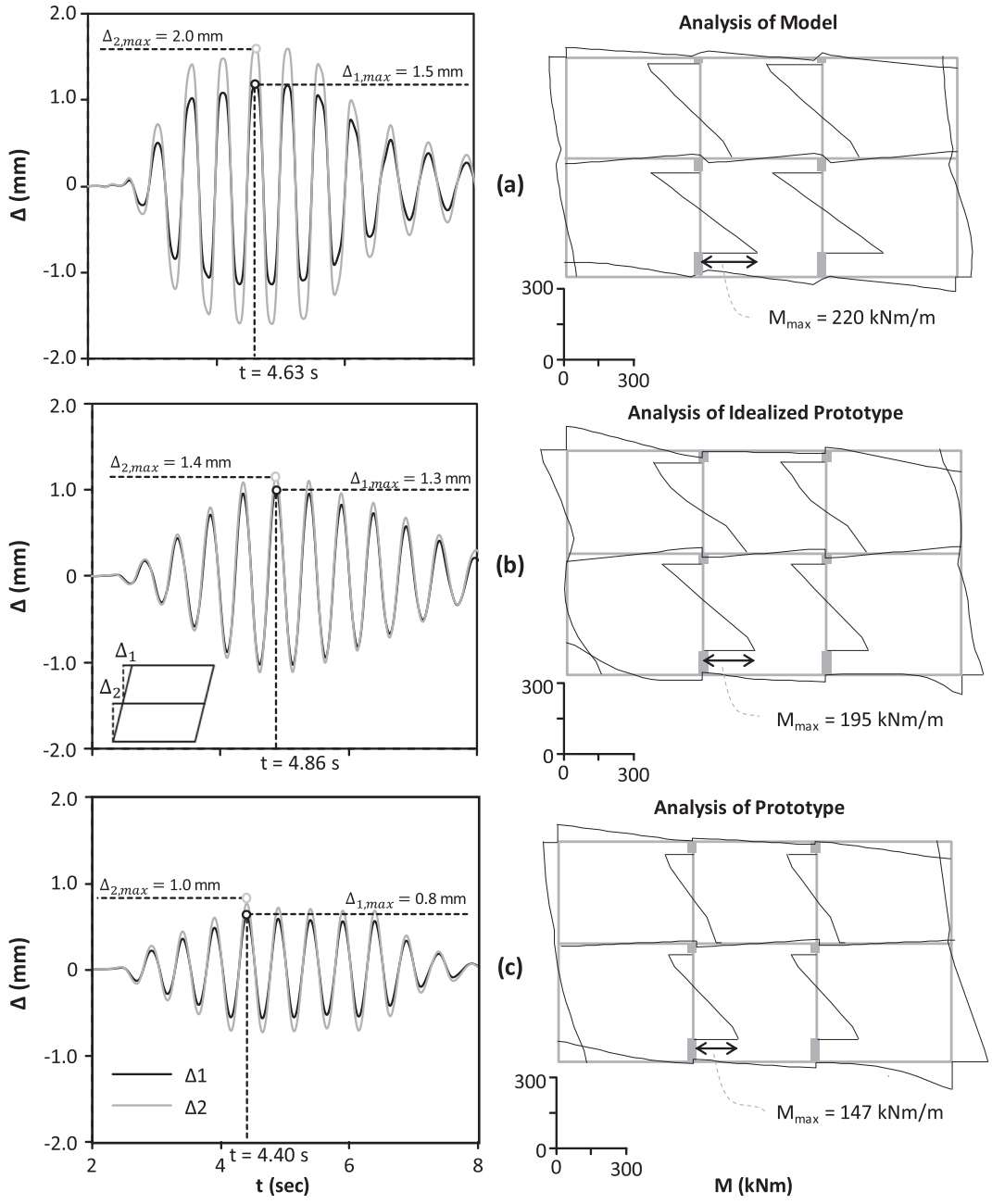

Fig. 21. Comparison of model to idealized prototype and prototype in terms of racking deformation (expressed through storey drift) and bending moments of structural members for sin sweep f=2 Hz seismic excitation: (a) analysis of model, including comparison to experimental measurements; (b) analysis of idealized prototype; and (c) analysis of prototype (all results are shown in prototype scale).

Fig. 21 compares the response of the *model* to that of the *idealized prototype* and of the *prototype*, in terms of racking deformation (expressed by the inter-storey drift Δ) and maximum bending moments of structural members (for the sin sweep of f=2 Hz seismic excitation). By comparing the *idealized prototype* to the *model*, the role of scale effects can be quantified. The comparison of the *prototype* to the *idealized prototype* provides insights on the simplification with respect to the soil profile (multi-layered vs. idealized). To allow for direct comparisons, all results are shown in prototype scale. The racking deformation of the metro station is qualitatively similar for all three cases, but of course, there are quantitative differences. The maximum lower-storey drift $\Delta_{2,max}$ is consistently larger than that of the upper storey $\Delta_{1,max}$, which can only partly be attributed to the larger height (by 17%, see Fig. 1) of the lower stoery of the station. In terms of drift ratio $\Delta_r = \Delta/H_s$ (where H_s is the height of the corresponding storey), the differences are smaller, but the conclusion remains the same. Interestingly, the largest $\Delta_{2,max}$ = 2 mm is observed for the *model* (Fig. 21**a**), compared to 1.4 mm of the *idealized prototype* (Fig. 21**b**), and 1.0 mm of the prototype (Fig. 21**c**). Since the *idealized prototype* maintains the relative stiffness of the model, this difference can only be attributed to scale effects related to the soil. With respect to the *prototype*, the racking deformation would be expected to be larger, given the smaller relative stiffness of the station. The reduced (by 30%) $\Delta_{2,max}$ is therefore attributed to the detailed modelling of the multiple soil layers of the prototype and the increased interface friction angle $\delta = \varphi = 30^{\circ}$.

The computed bending moments are also qualitatively similar across scales (*model*, *idealized prototype*, and *prototype*). As expected, the maximum bending moment M_{max} is observed at the base of the lower-storey (internal) columns. Consistent with the previous observations regarding $\Delta_{2,max}$, the largest M_{max} of 220 kNm/m is observed for the

model (Fig. 21**a**), being lower for *idealized prototype* (M_{max}=195 kNm/m, Fig. 21**b**), and even lower for the *prototype* (M_{max}=147 kNm/m, Fig. 21**c**). Despite the quantitative differences across scales, the key conclusion remains the same: the base of the lower-storey columns is the most vulnerable and should be carefully reinforced to avoid failure, similar to that of the Daikai metro station.

6. Summary and conclusions

This paper has presented a *combined* experimental and numerical study of the seismic performance of a typical two-storey three-span Shanghai Metro station in soft soil. Although scale effects can be effectively addressed by centrifuge modelling, detailed simulation of the structural system of such a Metro station (especially of internal columns) would be particularly challenging due to capacity limitations. Within this context, 1g shaking table testing was conducted, allowing simulation of internal structural members in adequate detail. This was achieved by using granular concrete (a mixture of cement, sand, lime, and water) and galvanized steel wires for reinforcement. Thanks to its lower compressive strength, granular concrete allows maintaining similarity in terms of bending moment capacity.

To remedy the problem of scale effects (to the extent possible), "synthetic" model soil (a mixture of sawdust and dry sand) was used for the shaking table experiments, along with similitude relations that were derived through dynamic equilibrium. The multi-layered *prototype* soil was idealized as a single *model* soil layer. The V_s distribution of the *idealized prototype* was selected by matching that of the *prototype*. The properties of the *synthetic model soil* were adjusted to satisfy the derived similitude relations and match the G_0 distribution with depth of the *idealized prototype*. The target stiffness and density were attained by adjusting the proportions of the two mixture components (sand and sawdust). By adding a reduced density component to the mixture (sawdust), the produced synthetic soil satisfies similarity and G_0 distribution, being substantially lighter than real soil, thus offering the possibility to conduct the experiments using a larger geometry scale.

Although such *synthetic model soil* has been used in previous studies, the transferability of the 1 g shaking table test results to prototype conditions has not been fully understood. Aiming to quantify the degree of such transferability, the 1 g shaking table experiments were subsequently modelled with nonlinear finite elements (FE), assuming the properties of the *synthetic model soil*. An extended pressure-dependent kinematic hardening constitutive model was employed to capture nonlinear soil response. The model was calibrated for the *synthetic model soil* using the results of resonant column and direct shear tests, which were also conducted as part of this study. In this way, the 1 g shaking table tests served as a benchmark for model validation. The FE model was shown to compare well with the shaking table tests in terms of acceleration time histories and amplification. Larger discrepancies were observed when examining soil pressures on the station sidewall, which, however, may be due to measurement errors rather than modelling inaccuracies.

Then, the validated FE model was used to predict the seismic response of the metro station in *prototype* scale, thus allowing indirect transfer of the results from *model* to *prototype* scale. Moreover, the role of scale effects was quantified by comparing *prototype*-scale results to those of *model*-scale. Going from the model "*back to reality*" was performed in two steps: (1) from *model* to *idealized prototype* (same single-layer soil profile, but prototype dimensions); and (2) from *idealized prototype* to real *prototype* (actual multi-layered soil). The extended pressure-dependent kinematic hardening model was calibrated using the in situ-measured (down-hole tests) V_s profile in combination with laboratory-measured (resonant column tests) $G-\gamma$ curves, both conducted as part of this study. Moving from *model* to *prototype* scale, the racking deformation of the metro station was shown to be qualitatively similar. The drift of the lower-storey was found to be consistently larger than that of the upper storey, something which is only partly due to its larger height. The drift was reduced by almost 50% going from *model* to *prototype* scale, which is partly due to scale effects and partly due to the differences between the idealized single soil layer of the experiment and the multiple soil layers encountered in reality.

The computed bending moments were also found to be qualitatively similar across scales. Consistent with the racking drift, M_{max} was found to reduce by rougly 30% going from *model* to *prototype* scale. The maximum bending moment M_{max} was observed at the base of the lower-storey columns, confirming that this is the most vulnerable section of such Metro stations, as was the case with the collapse of the Daikai Metro station during the 1995 Kobe earthquake.

CRediT authorship contribution statement

Weifeng Wu: Conceptualization, Methodology, Software, Formal analysis, Investigation, Data curation, Writing - original draft, Visualization. **Shiping Ge:** Conceptualization, Resources, Writing - review & editing, Supervision, Project administration, Funding acquisition. **Yong Yuan:** Validation, Resources, Writing - review & editing, Supervision, Project administration, Funding acquisition. **Wenqi Ding:** Resources, Writing - review & editing, Supervision, Project administration, Funding acquisition. **Ioannis Anastasopoulos:** Conceptualization, Methodology, Validation, Resources, Writing - original draft, Writing - review & editing, Supervision, Project administration.

Acknowledgement

We would like to acknowledge financial support by the National Key Research and Development Plan of China (2017YF0806004 & 2017YFC1500703 & 2018YFC0809602 & 2018YFC1504305) and Shanghai Metro Research Project (JS-KY17R031-6). The first author would like to acknowledge China Scholarship Council, China (CSC201806260187) for providing a scholarship for this work.

References

Abuhajar, O., El Naggar, H., Newson, T., 2015. Experimental and numerical investigations of the effect of buried box culverts on earthquake excitation. Soil Dyn. Earthquake Eng. 79, 130–148.
Adamidis, O., Madabhushi, S.P., 2017. Deformation mechanisms under shallow foundations on liquefiable layers of varying thickness. Géotechnique 68 (7), 602–613.
Ambraseys, N.N., 1959. A note on the response of an elastic overburden of varying rigidity to an arbitrary ground motion. Bull. Seismol. Soc. Am. 49, 211–220.
An, X., Shawky, A.A., Maekawa, K., 1997. The collapse mechanism of a subway station during the Great Hanshin earthquake. Cem. Concr. Compos. 19, 241–257.
Anastasopoulos, I., Gazetas, G., Asce, M., Bransby, M.F., Davies, M.C.R.R., El Nahas, A., 2007. Fault rupture propagation through sand: Finite-element analysis and validation through centrifuge experiments. J. Geotech. Geoenviron. Eng. 133, 943–958.
Anastasopoulos, I., Gelagoti, F., Kourkoulis, R., Gazetas, G., 2011. Simplified Constitutive Model for Simulation of Cyclic Response of Shallow Foundations: Validation against Laboratory Tests. J. Geotech. Geoenviron. Eng. 137, 1154–1168.
Armstrong, P.J., Frederick, C.O., 1966. A mathematical representation of the multiaxial bauschinger effect. CEGB Report, No. RD/B/N 731.
Bilotta, E., Lanzano, G., Madabhushi, S.G., Silvestri, F., 2014. A numerical round robin on tunnels under seismic actions. Acta Geotech. 9 (4), 563–579.
CAMET (China Association of Metros). 2019. Report on statistics and analysis of urban rail transit 2018. China Metros. 04, 16–34. [in Chinese].
Chen, J., Yu, H., Bobet, A., Yuan, Y., 2020a. Shaking table tests of transition tunnel connecting TBM and drill-and-blast tunnels. Tunn. Undergr. Space Technol. 96, 103–197.
Chen, J., Yuan, Y., Yu, H., 2020b. Dynamic response of segmental lining tunnel. Geotech. Test. J. 43 (3).
Chen, Z., Liang, S., Shen, H., He, C., 2018. Dynamic centrifuge tests on effects of isolation layer and cross-section dimensions on shield tunnels. Soil Dyn. Earthquake Eng. 109, 173–187.
Chen, Z., Liu, Z., 2019. Effects of pulse-like earthquake motions on a typical subway station structure obtained in shaking-table tests. Eng. Struct. 198, 109557.
CREEGC (China Railway Eryuan Engineering Group Co. Ltd). 2014. Preliminary design of Shanghai metro line 14, General specification, Shanghai. [In Chinese].
Cilingir, U., Madabhushi, S.P.G., 2011. Effect of depth on the seismic response of square tunnels. Soils Found. 51, 449–457.
Faccioli, E., Paolucci, R., Vanini, M. (Eds.), 1999. TRISEE: 3D site effects and soil-foundation interaction in earthquake and vibration risk evaluation. European Commission

Publication.
Gazetas, G., 1982. Vibrational characteristics of soil deposits with variable wave velocity. Int. J. Numerical Anal. Methods Geomech. 6, 1–20.
Gerolymos, N., Gazetas, G., Tazoh, T., 2005. Seismic response of yielding pile in non-linear soil. In: Proc. 1st Greece-Japan Workshop, Seismic Design, Observation, and Retrofit of Foundations. National Technical University of Athens, Greece, pp. 25–36.
Giannakos, S., Gerolymos, N., Gazetas, G., 2012. Cyclic lateral response of piles in dry sand: Finite element modeling and validation. Comput. Geotech. 44, 116–131.
Gibson, A.D., 1996. Physical scale modeling of geotechnical structures at one-G. California Institute of Technology.
Hardin, B., Richart, F., 1963. Elastic wave velocities in granular soils. J. Soil Mech. Found. Div. 89, 33–66.
Hashash, Y., Hook, J., Schmidt, B., John, I., Yao, C., 2001. Seismic design and analysis of underground structures. Tunn. Undergr. Space Technol. 16 (4), 247–293.
Hibbitt, H., Karlsson, B., Pawtucket, P.S.-, Island, R., USA, U., 2012, U., 2012. ABAQUS theory manual, version 6.12.
Huo, H., Bobet, A., Fernández, G., Ramírez, J., 2005. Load transfer mechanisms between underground structure and surrounding ground: evaluation of the failure of the daikai station. J. Geotech. Geoenviron. Eng. 131, 1522–1533.
Iai, S., 1989. Similitude for shaking table tests on soil-structure-fluid model in 1g gravitational field. Soils Found. 29, 105–118.
Iida, H., Hiroto, T., Yoshida, N., Iwafuji, M., 1996. Damage to daikai subway station. Soils Found. 36, 283–300.
Ishibashi, I., Zhang, X., 1993. Unified dynamic shear moduli and damping ratios of sand and clay. Soils Found. 33, 182–191.
Ishibashi, T., Okamura, H., 1997. Study on the design earthquake resistance and degree of earthquake damage of reinforced concrete viaducts. Cem. Concr. Compos. 19, 193–201.
Kondner, R., 1963. Hyperbolic stress-strain response: cohesive soils. J. Soil Mech. Found. Div. 89 (1), 115–144.
Kramer, S.L., 1996. Geotechnical Earthquake Engineering. Upper Saddle River, N.J., Prentice Hall.
Kutter, B. L., Martin, G., Hutchinson, T., Harden, C., Gajan, S., Phalen, J. 2003. Workshop on modeling of nonlinear cyclic load-deformation behavior of shallow foundations. Pacific Earthquake Engineering Research Center, PEER report 2005/14.
Labuz, J.F., Theroux, B., 2005. Laboratory calibration of earth pressure cells. Geotech. Test. J. 28, 188–196.
Langhaar, H.L., 1951. Dimensional Analysis and Theory of Models. Wiley, New York.
Lanzano, G., Bilotta, E., Russo, G., Silvestri, F., 2015. Experimental and numerical study on circular tunnels under seismic loading. Eur. J. Environ. Civil Eng. 19, 539–563.
Lemaitre, J., Chaboche, J.-L., 1990. Mechanics of solid materials. Cambridge University Press, Cambridge, UK.
Loli, M., Knappett, J.A., Brown, M.J., Anastasopoulos, I., Gazetas, G., 2014. Centrifuge modeling of rocking-isolated inelastic RC bridge piers. Earthquake Eng. Struct. Dyn. 43, 2341–2359.
Lu, C.C., Hwang, J.H., 2019. Nonlinear collapse simulation of Daikai Subway in the 1995 Kobe earthquake: Necessity of dynamic analysis for a shallow tunnel. Tunn. Undergr. Space Technol. 87, 78–90.
Owen, G.N., 1981. Earthquake Engineering of Large. Underground Structures.
Pitilakis, K., Tsinidis, G., 2014. Performance and Seismic Design of Underground Structures. In: Earthquake geotechnical engineering design. Springer, Cham, pp. 279–340.
Ranf, R.T., Eberhard, M.O., Berry, M.P., 2001. Pacific Earthquake Engineering Research Center. University California, Berkeley.
Roscoe, K.H., 1968. Soils and model tests. J. Strain Anal. 3 (1), 57–64.
Shawky, A., Maekawa, K., 1996. Nonlinear Response of Underground RC Structures under Shear. Doboku Gakkai Ronbunshu 195–206 [In Japanese].
Shen, Y., Wang, Z., Yu, J., Zhang, X., Gao, B., 2020. Shaking table test on flexible joints of mountain tunnels passing through normal fault. Tunn. Undergr. Space Technol. 103–299.
Stamos, A.A., Beskos, D.E., 1995. Dynamic analysis of large 3-D underground structures by the bem. Earthquake Eng. Struct. Dyn. 24, 917–934.
Tsinidis, G., Pitilakis, K., Trikalioti, A.D., 2014. Numerical simulation of round robin numerical test on tunnels using a simplified kinematic hardening model. Acta Geotech. 9 (4), 641–659.
Wang, J.N., 1993. Seismic design of tunnels: a state-of-the-art approach, Parsons, Brinckerhoff, Quade and Douglas Inc. New York, NY, USA, New York.
Wood, D.M., Crewe, A., Taylor, C., 2002. Shaking table testing of geotechnical models. Int. J. Phys. Modelling Geotech. 2, 01–13.
Xianfeng, M., Guobo, W., Jun, W., Qianqian, J., 2017. Experimental study on the seismic response of subway station in soft ground. J. Earthquake Tsunami 11, 1–27.
Yan, X., Yu, H., Yuan, Y., Yuan, J., 2015. Multi-point shaking table test of the free field under non-uniform earthquake excitation. Soils Found. 55, 985–1000.
Yu, H., Yan, X., Bobet, A., Yuan, Y., Xu, G., Su, Q., 2018. Multi-point shaking table test of a long tunnel subjected to non-uniform seismic loadings. Bull. Earthq. Eng. 16, 1041–1059.
Yuan, Y., Yu, H., Li, C., Yan, X., Yuan, J., 2018. Multi-point shaking table test for long tunnels subjected to non-uniform seismic loadings – Part I: Theory and validation. Soil Dynamics Earthquake Eng. 108, 177–186.
Zhang, J., Yuan, Y., Bao, Z., Yu, H., Bilotta, E., 2019a. Shaking table tests on the intersection of cross passage and twin tunnels. Soil Dyn. Earthquake Eng. 124, 136–150.
Zhang, J., Yuan, Y., Yu, H., 2019b. Shaking table tests on discrepant responses of shaft-tunnel junction in soft soil under transverse excitations. Soil Dyn. Earthquake Eng. 120, 345–359.
Zhao, H., Yuan, Y., Ye, Z., Yu, H., Zhang, Z., 2019. Response characteristics of an atrium subway station subjected to bidirectional ground shaking. Soil Dyn. Earthquake Eng. 125, 105737.